

10/16/96
F. C. Starnes Jr.

NONLINEAR ANALYSIS OF THE SPACE SHUTTLE SUPER-LIGHTWEIGHT EXTERNAL FUEL TANK

by

Michael P. Nemeth, Vicki O. Britt, Timothy J. Collins, and James. H. Starnes, Jr.
NASA Langley Research Center
Hampton, Virginia 23681-0001

Presented at the AIAA / ASME / ASCE / AHS / ASC Structures,
Structural Dynamics, and Materials Conference

AIAA Paper No. 96-1552

Salt Lake City, Utah
April 15-17, 1996

NONLINEAR ANALYSIS OF THE SPACE SHUTTLE SUPER-LIGHTWEIGHT EXTERNAL FUEL TANK

Michael P. Nemeth*, Vicki O. Britt**, Timothy J. Collins†, and James. H. Starnes, Jr.‡
NASA Langley Research Center
Hampton, Virginia 23681-0001

Abstract

Results of buckling and nonlinear analyses of the Space Shuttle External Tank super-lightweight liquid-oxygen (LO_2) tank are presented. Modeling details and results are presented for two prelaunch loading conditions and for two full-scale structural tests that were conducted on the original External Tank. These results illustrate three distinctly different types of nonlinear response for thin-walled shells subjected to combined mechanical and thermal loads. These nonlinear response phenomena consist of bifurcation-type buckling, short-wavelength nonlinear bending, and nonlinear collapse associated with a limit point. For each case, the results show that accurate predictions of nonlinear behavior generally require a large-scale, high-fidelity finite element model. Results are also presented that show that a fluid-filled launch-vehicle shell can be highly sensitive to initial geometric imperfections. In addition, results presented for two full-scale structural tests of the original standard-weight External Tank suggest that the finite element modeling approach used in the present study is sufficient for representing the nonlinear behavior of the super-lightweight LO_2 tank.

Introduction

The new era of cooperation in space between the United States and Russia has created a requirement for the Space Shuttle to reach a 51.6-degree high-inclination orbit. Currently, achieving this orbit requires the payload of the Orbiter to be reduced by approximately 10,000 pounds. To recover most of the lost payload, NASA is presently developing a new lightweight external fuel tank for the Space Shuttle that is primarily made from an aluminum-lithium alloy. This new design is referred to as the Super-Lightweight External Tank (SLWT) and is expected to weigh approximately 58,000 lbs which is approximately 8,000 lbs lighter than the lightweight aluminum external tank currently in service.

* Senior Research Engineer, Structural Mechanics Branch. Senior Member, AIAA.

** Aerospace Engineer, Structural Mechanics Branch. Member, AIAA.

† Aerospace Engineer, Structural Mechanics Branch.

‡ Head, Structural Mechanics Branch. Fellow, AIAA.

Copyright © 1996 by the American Institute of Aeronautics and Astronautics, Inc. No copyright is asserted in the United States under Title 17, U.S. Code. The U.S. Government has a royalty-free license to exercise all rights under the copyright claimed herein for government purposes. All other rights are reserved by the copyright owner.

An important consideration in the design of the SLWT is the nonlinear behavior of the thin-walled regions of the structure that have compressive stresses. Local or global buckling of the shell wall can cause the thermal protection system (TPS) to separate from the tank which could cause the vehicle to fail. As part of a plan to assure that the design does not have a shell-wall instability response, accurate predictions of the nonlinear response of the SLWT are needed. Accurate predictions of the nonlinear response of the SLWT require a large-scale, high-fidelity finite element model to represent the complex structural details of the SLWT, and a robust nonlinear shell analysis capability that can predict local and general instability buckling modes.

One of the components of the SLWT that has significant compressive stresses is the liquid-oxygen (LO_2) tank. A primary goal of the present paper is to present results that give an indication of how much additional load, beyond the operational loads for two critical prelaunch loading conditions, the LO_2 tank can withstand before buckling or exhibiting severe bending gradients. Toward that goal, results of nonlinear analyses of the LO_2 tank conducted by NASA Langley Research Center personnel for the two prelaunch loading conditions are presented in the present paper. In addition, results are presented for two full-scale structural tests of the original standard-weight tank (SWT) LO_2 tank configuration, that differs primarily in wall thickness, weight, and material type from the SLWT LO_2 tank. These results are included in the present paper to demonstrate that the finite element modeling approach used in the present study yields accurate representations of the nonlinear structural response of the SLWT LO_2 tank.

A second goal of the present paper is to present results that illustrate some types of nonlinear behavior, and their sensitivity to initial geometric imperfections, that may be encountered in the design of liquid-fuel launch vehicles. Thus, results for the two prelaunch loading conditions and the full-scale structural tests are presented that illustrate three distinctly different types of nonlinear responses of thin-walled shells subjected to combined mechanical and thermal loads. The nonlinear response for the first prelaunch loading condition is characterized by a bifurcation-type buckling response that is insensitive to initial geometric imperfections and exhibits substantial postbuckling load carrying capacity. In contrast, the nonlinear response for the second

prelaunch loading condition is characterized by a short-wavelength bending gradient that grows in amplitude with increasing load in a stable manner. The nonlinear responses for the two full-scale structural tests are characterized by a limit-point response of a doubly curved shell segment that buckles locally. The magnitude of the load corresponding to the limit point is shown to be sensitive to initial geometric imperfections in the LO₂ tank.

For each of the three different nonlinear response phenomena presented in the present paper, the modeling approach and implementation used to develop a high-fidelity finite element model that adequately represents the behavior is discussed. An overview of the SLWT LO₂ tank and Intertank structure and loading conditions is presented, the analysis code and finite element modeling details are discussed, and the results of the linear bifurcation buckling analyses and the nonlinear analyses are presented. Although the modeling approach and implementation presented in the present paper are for a specific launch vehicle, they represent a general method that can be applied to the design of future liquid-fuel launch vehicles.

Overview of the SLWT Structure

The Space Shuttle consists of the Orbiter, two Solid Rocket Boosters (SRBs), and the External Tank (ET) as shown in Fig. 1. The External Tank consists of a liquid-oxygen (LO₂) tank, a liquid-hydrogen (LH₂) tank, and an intermediate structure called the Intertank (see Fig. 1). The Intertank transmits the weight of the fuel, the ET structural weight, and the Orbiter weight to the SRBs prior to launch, and transmits thrust loads from the SRBs and the Orbiter to the ET during ascent. The SLWT LO₂ tank is a thin-walled monocoque shell that is primarily made of 2195 aluminum-lithium alloy. The LO₂ tank is approximately 49 ft long and has a maximum diameter of approximately 27.5 ft, as indicated in Fig. 2. The LO₂ tank consists of a forward ogive section that is made from eight gore panels, an aft ogive section that is made from twelve gore panels, a cylindrical barrel section that is made from four barrel panels, and an aft elliptical dome section that is made from twelve gore panels. The coordinate systems used to locate the elements of the LO₂ tank and the Intertank are also shown in Fig. 2. The coordinates (XT, Y, Z) are typically referred to as the global coordinate system of the ET, and axial positions along the tank are indicated by the coordinate value of XT in units of inches. For example, the junction between the forward and aft ogives is indicated by writing XT = 536.74. Cylindrical coordinates are also used and are given by (r, θ, XT) where a positive value of θ is measured from

the positive Z-axis toward the positive Y-axis as shown in Fig. 2.

The LO₂ tank also has a forward T-ring and an aft Y-ring frame that supports a slosh baffle that prevents the fuel from sloshing during ascent. The slosh baffle is a lightweight (approximately 455 lbs.), thin-walled structure that is supported by two deep, thin-walled rings at each end that attach to the forward T-ring and the aft Y-ring frame. Other parts of the LO₂ tank include a nonstructural nose cone, a forged forward ogive fitting and cover plate, an aft spherical dome cap that contains the LO₂ suction fitting and a covered manhole, and a vortex baffle attached to the base of the aft dome cap. The LO₂ tank gore and barrel panels are stretch formed, chemically milled, and then welded together. The panels are fabricated with substantial thickness tailoring to reduce structural weight. The panels are made somewhat thicker at the welds to form a stiffener-like region that is used as a weld land. The primary role of the weld lands is to compensate for reduction in shell-wall strength due to welding. The weld lands are tapered in thickness and width along their length to reduce weight and to alleviate stress concentrations in the shell due to abrupt changes in thickness.

The Intertank is a right circular cylinder that is made from 2090 and 7075 aluminum alloys and is shown in Fig. 3. It is approximately 22.5 ft long and has a diameter of approximately 27.5 ft. The Intertank consists of six 45-degree curved panels that are stiffened longitudinally with external hat stiffeners and are referred to herein as skin-stringer panels. The Intertank also has two massive 45-degree curved panels located perpendicular to the Y-axis of the Intertank (see Fig. 3) that are stiffened longitudinally with integrally machined external blade stiffeners and are referred to herein as thrust panels. These eight panels are assembled into the Intertank with mechanical fasteners, and are attached to five large internal ring frames, a forward flange, and an aft flange. Lateral-torsional deflection of the ring frames is suppressed by longitudinal straps referred to herein as roll ties. The main central ring frame, two thrust panel longerons, and the thrust panels are connected to each end of a tapered beam, referred to herein as the SRB beam (see Fig. 3). The SRB beam spans the diameter of the Intertank along the Y-axis and has a maximum depth (in the XT direction) of approximately 43 in. at its midspan. Forged fittings, referred to herein as SRB thrust fittings, that are incapable of transmitting moments are fastened to the ends of the SRB beam. The primary role of the thrust panels is to diffuse the large axial loads introduced by the solid rocket boosters into the Intertank and then into the LO₂ tank shell wall. The SRB beam is provided to compensate for the eccentricity of the concentrated loads introduced by the solid rocket

boosters. The SRB beam also supports the loads normal to the Intertank (parallel to the SRB beam) at the SRB attachment points. The Intertank also has a 46-in.-high by 52-in.-wide frame-reinforced nonstructural access door that is located along the cylinder generator at approximately $\theta = 146$ degrees.

Critical Prelaunch Loading Conditions

Several critical SLWT loading conditions have been identified by the members of the SWLT team at the NASA George C. Marshall Space Flight Center and at the Lockheed-Martin Manned Space Systems Division. The general characteristics of the critical loads are indicated in Fig. 4. These loads consist of the wind or aerodynamic pressure loads, the structural weight or inertia, the pressure exerted on the shell wall by the LO₂, the ullage pressure inside the tank, the interface forces exerted by each SRB (indicated by the vectors **R**₁ and **R**₂ in Fig. 4), the interface forces between the Intertank and the LH₂ tank (indicated by the vectors **F** and **M** in Fig. 4), and the thermally induced loads associated with the cryogenic temperatures.

Two critical loading conditions addressed herein correspond to prelaunch fueling conditions that occur when the Space Shuttle is on the launch pad. Prior to launch, the LH₂ tank is filled with LH₂, and then the LO₂ tank is filled with LO₂. The first loading condition considered herein corresponds to a full LH₂ tank and an empty LO₂ tank. For this condition, there is no pressure and no temperature change in the LO₂ tank. However, the lower 45 in. of the Intertank is subjected to an axisymmetric uniform through-the-thickness temperature field that varies linearly from -423 °F, where the Intertank is attached to the LH₂ tank, to +50 °F at the top of the LH₂ tank forward dome. The nominal ambient temperature of the LO₂ tank and the Intertank prior to fueling is +50 °F. The SRB interface forces are given by

$$\begin{aligned}\mathbf{R}_1 &= -224.092 \mathbf{i} - 52.223 \mathbf{j} - 28.954 \mathbf{k} \text{ kips} \\ \mathbf{R}_2 &= -343.624 \mathbf{i} + 48.261 \mathbf{j} - 30.754 \mathbf{k} \text{ kips}\end{aligned}$$

where the vectors **R**₁ and **R**₂ are shown in Fig. 4 and where **i**, **j**, and **k** are standard orthonormal base vectors associated with the XT, Y, and Z axes, respectively. Similarly, the interface force and moment between the Intertank and the LH₂ tank are given by

$$\begin{aligned}\mathbf{F} &= 541.593 \mathbf{i} + 9.614 \mathbf{j} + 63.494 \mathbf{k} \text{ kips} \\ \mathbf{M} &= -310.500 \mathbf{i} + 10,715.745 \mathbf{j} + 16,828.589 \mathbf{k} \text{ in.-kips.}\end{aligned}$$

The LO₂ tank is also subjected to wind pressure that has a resultant force given by $-5.652 \mathbf{j} - 3.786 \mathbf{k}$ kips.

The second prelaunch loading condition considered herein corresponds to full LH₂ and LO₂ tanks, but without ullage pressure. For this condition, the LO₂ tank is filled to XT = 447 (see Fig. 2) which corresponds to a depth of approximately 43 feet. For this case, the hydrostatic pressure distribution in the LO₂ tank is essentially axisymmetric and the temperature distribution in the LO₂ tank and Intertank is axisymmetric and uniform through-the-thickness as shown in Fig. 5. The specific weight of the LO₂ used in the present study is 0.04123 lbs/in.³ and the maximum hydrostatic pressure is approximately 21 psig at the bottom of the tank. The corresponding weight of the LO₂ is approximately 1,348 kips.

The temperature field for the LO₂ tank shown in Fig. 5 has a uniform value of -297 °F between XT = 447 and XT = 852.8, but varies from a value of -150 °F at the nose to -297 °F at the free surface of the LO₂ (XT = 447). The Intertank is subjected to an axisymmetric uniform through-the-thickness temperature field that varies in a piecewise linear manner from -423 °F to +50 °F and then to -297 °F as the Intertank is traversed from XT = 1129 to XT = 852.8. The temperature field shown in Fig. 5 represents the changes in the temperature distribution that occur from the nominal prefueling temperature of +50 °F.

The SRB interface forces for the second prelaunch loading condition are given by

$$\begin{aligned}\mathbf{R}_1 &= -906.447 \mathbf{i} - 105.605 \mathbf{j} - 30.502 \mathbf{k} \text{ kips} \\ \mathbf{R}_2 &= -1035.789 \mathbf{i} + 108.128 \mathbf{j} - 32.557 \mathbf{k} \text{ kips}\end{aligned}$$

Likewise, the interface force and moment between the Intertank and the LH₂ tank are given by

$$\begin{aligned}\mathbf{F} &= 568.113 \mathbf{i} + 3.014 \mathbf{j} + 66.913 \mathbf{k} \text{ kips} \\ \mathbf{M} &= -354.488 \mathbf{i} + 11,249.318 \mathbf{j} + 19,443.206 \mathbf{k} \text{ in.-kips.}\end{aligned}$$

and the LO₂ tank is subjected to a wind load with a resultant force given by $-5.537 \mathbf{j} - 3.854 \mathbf{k}$ kips.

Analysis Code and Finite Element Modeling

The results of the linear bifurcation buckling and nonlinear analyses presented herein were obtained with the STAGS nonlinear structural analysis code for general shells (Ref. 1). The finite element models of the SLWT used in the present study are very complex

models and include many structural details and the skin thickness variations or tailoring used to reduce structural weight. STAGS was chosen for analyzing the SLWT because of its robust state-of-the-art nonlinear-equation solution algorithms and its general user-input capability that is convenient for modeling branched shells typically used for launch vehicles. In particular, STAGS uses both the full and modified Newton methods to obtain an accurate nonlinear solution, and large rotations in the shell are represented by a co-rotational algorithm at the element level. The Riks arc-length projection method is used to continue a solution past limit points. STAGS permits complex geometries, loading conditions, and initial geometric imperfections to be modeled in a direct manner by the use of user-written subroutines that are essentially independent of the mesh discretization. For example, these user-written subroutines allow the user to define reference surface geometries; tapered shell walls and stiffener cross-sections; and complex nodal force, temperature, and pressure distribution functions in a direct manner using statements of the FORTRAN computer language. This feature greatly simplified the definition of the finite element models and the mesh convergence studies conducted in the present study. A description of how the features of STAGS were used in the present study to model the SLWT LO₂ tank and Intertank are presented in this section. In addition, details of how the prelaunch loads are simulated are also presented.

In modeling the SLWT LO₂ tank and the Intertank, several assumptions were made to simplify the finite element models. Limited parametric studies were made to determine the adequacy of the assumptions and simplifications. For each case, the modeling assumptions used in the present study to simplify the finite element models were found to be acceptable for analyzing the nonlinear behavior of the SLWT LO₂ tank.

Modeling Details for the LO₂ Tank

One very useful method for finite-element-mesh generation in STAGS involves defining the number of rows and columns of nodes in a segment of a specific type of shell (reference surface) unit such as a cylinder, a cone, or a sphere. STAGS has a library of several different predefined shell units that are based on a specific type of surface parametric representation. For instances where a different surface parametric representation for one of the shell units in the STAGS library is needed, or when a type of shell unit is needed that is not in the STAGS library, the surface information is input into STAGS using the user-written subroutine called LAME. For the forward and aft ogive sections of the SLWT LO₂ tank, a parametric

representation defined in terms of the global circumferential coordinate θ (defined in Fig. 2) and a local axial coordinate of the shell unit is put into LAME. The ogive geometry is based on a nominal 612.0-inch meridional radius of curvature and a 165.5-inch maximum polar radius of curvature. The reference surfaces for the forward ogive fitting and cover plate indicated in Fig. 2 are input as an ogive segment and a circular segment of a plane, respectively. The ogive segment has an axial (XT) length of 4 in. and polar radii of 25.676 in. and 28.950 in. at XT = 371 and XT = 375, respectively. Similarly, the flat reference surface of the cover plate has a radius of 25.676 in.

The reference surface for the barrel section of the LO₂ tank is input as a right circular cone with polar radii equal to 165.359 in. and 165.373 in. at XT = 748.67 and XT = 843, respectively, and the reference surface for the aft dome section is input as a truncated ellipsoid attached to a smaller spherical cap. To simplify the model, the LO₂ suction fitting and covered manhole are neglected in defining the reference surface (and mesh) of the spherical cap. This simplification is based on the reasoning that the local details of the spherical cap will have a negligible effect on the behavior of the ogives and the barrel. The ellipsoid has a 165.50-inch semi-major axis in the radial direction and a 124.125-inch semi-minor axis in the axial direction. The spherical dome cap has a 70.0-inch polar radius at XT = 951.526, a 211.855-inch spherical radius, and a 11.9-inch axial length. The aft Y-ring section of the tank indicated in Fig. 2 is modeled with four reference surfaces that connect the barrel to the aft dome and to the Intertank. The reference surface that connects the barrel to the Intertank is a 165.373-inch-radius cylinder that is 9.8 in. long. Two conical reference surfaces connect the barrel to the aft dome. The first is an 8.0-inch-long cone with outer and inner polar radii equal to 165.373 in. and 164.72 in. at XT = 843 and XT = 851, respectively, and the second is a 4.273-inch-long cone with outer and inner polar radii equal to 164.72 in. and 164.08 in. at XT = 851 and XT = 855.273, respectively. The fourth reference surface is a very short and essentially rigid cone that connects the aft end of the cylindrical surface to the intersection of the two conical sections. This cone is included in the model to represent adequately the stiffness of the Y-ring section where the shell segments join in order to prevent the Y-ring from passing through the adjacent shell walls during deformation. This modeling detail is also used to eliminate large artificial bending gradients in the Y-ring shell wall that can cause convergence problems in the numerical solution of the nonlinear equations.

The SLWT LO₂ tank shell wall is chemically milled to reduce structural weight and has a highly variable thickness distribution. In the forward ogive, the thicknesses vary from 0.080 in. to 0.157 in. in both

the meridional and circumferential directions. Similarly, in the aft ogive and barrel sections the thicknesses vary from 0.081 in. to 0.190 in. and from 0.140 in. to 0.385 in., respectively. In the aft dome the thicknesses vary from 0.088 in. to 0.125 in. This complex thickness distribution and corresponding wall eccentricities are input into the STAGS user-written subroutine WALL using FORTRAN statements. In addition, the LO₂ tank is thickened locally in several regions that support an external cable tray, and these local thicknesses are included in subroutine WALL.

Several meridional lines are shown in Fig. 2 that represent the weld lands of the gore and barrel panels forming the tank. These weld lands are substantially thicker than the adjacent shell wall and their thicknesses vary in the meridional direction. The weld lands are modeled as discrete beams of rectangular cross-section with variable width and depth. The variations in the weld-land cross-sectional geometry in the meridional direction are represented using a linear variation with the corresponding surface arc-length. The variable properties of the beams are input into STAGS using the user-written subroutine CROSS. The circumferential location of each weld land is specified to be at the column of nodes in the shell unit that is closest to its actual location. This approximation becomes more accurate when the circumferential mesh density is increased. Circumferential weld lands are located where the forward and aft ogives are connected, where the T-ring attaches to the aft ogive and barrel, where the Y-ring attaches to the barrel and the aft dome, and where the elliptical part of the aft dome connects to the spherical cap. The weld lands located at the aft end of the barrel and elliptical dome are modeled as discrete rings for convenience and all the other weld lands are modeled using shell elements. In addition, the two deep, thin-walled slosh baffle rings are modeled as discrete rings. The remainder of the slosh baffle is not included in the STAGS models since the stiffness and stability it provides to the slosh baffle rings is essentially included by modeling the slosh baffle rings as discrete rings.

Parts of the forward ogive fitting and the entire cover plate contain integrally machined stiffeners. These structures are modeled as an equivalent homogeneous orthotropic wall with the appropriate shell reference surface eccentricity. In addition, cutouts and other local details in the cover plate are neglected, and places in the ogive fitting and cover plate where the thickness is much larger than the nominal wall thickness are modeled using discrete rings.

Modeling Details for the Intertank

The reference surface for the Intertank is a 165.373-inch-radius right circular cylinder that is 270.35 in. long. The six skin-stringer panels of the Intertank consist of external hat stiffeners bonded to a variable thickness wall. The skin thicknesses (including primary doublers) range from 0.067 in. to 0.221 in. The hat stiffeners range in thickness from 0.045 in. to 0.063 in., are 2.50 in. deep, and taper in width from 2.57 in. at the shell wall to 1.38 in. at the top of the hat. The hat stiffener spacing is 7.20 in. The objective of the Intertank model is to provide an accurate representation of the overall Intertank stiffness so that load can be transferred to the LO₂ tank with as few finite element degrees of freedom as possible. To achieve this goal, the skin-stringer panels are modeled as an equivalent homogeneous orthotropic wall with a variable thickness that is eccentric to the shell reference surface. The equivalent homogeneous orthotropic wall properties are computed by STAGS using the "smeared stiffener" capability of the user-written subroutines WALL and CROSS. This model includes the effects of all the hat stiffeners and the primary skin doubler plates. Eight extruded stringers that are fastened to four of the panels are not included in the model as discrete beams, but are approximated in a conservative manner as hat stiffeners with a maximum thickness of 0.63 in. The variable wall properties are input into STAGS using the user-written subroutine WALL. Cutouts in the panels, including the access door and its frame, are neglected based on the rationale that their influence on the transfer of load into the LO₂ tank is small.

The two thrust panels of the Intertank are blade stiffened panels that are integrally machined from a single piece of aluminum alloy. A total of sixty-five skin thicknesses ranging from 0.090 in. in areas away from the central region of the panels to 2.062 in. in the area next to the SRB thrust fittings are used to model the thrust panels. A wall thickness of 2.062 in. is placed in the cutouts that house the SRB thrust fittings to facilitate load diffusion from the SRB beam to the thrust panels. The two internal longerons fastened to the thrust panels and the SRB beam, however, are neglected. Each panel has twenty-six variable-width blade stiffeners that are 2.06 in. deep. Thirty-six blade widths ranging from 0.180 in. to 1.050 in. are used to model the thrust panels. The thrust panels are modeled as an equivalent homogeneous orthotropic wall with variable thickness in a manner similar to the skin-stringer panels.

The five internal ring frames and two (forward and aft) flanges of the Intertank are modeled as discrete rings with variable and constant cross-sectional properties, respectively. For the ring frames, the section properties are modeled in a piecewise manner using constant

properties for each beam element connecting two adjacent nodes. Since the discrete ring model of the ring frames does not account for lateral-torsional cross-sectional deformations, the effect of the roll ties shown in Fig. 3 is implicitly included. The SRB beam is also modeled as a discrete beam using several beam elements to simulate its variable depth in a piecewise manner. The SRB beam is approximately 345 in. long and extends outboard of the shell reference surface to cause an eccentricity in the SRB interface forces of approximately 7 inches, as shown in Fig. 4. Load diffusion from the ends of the SRB beam to the shell wall of the thrust panels is facilitated by connecting the node at each end of the SRB beam to the adjacent nodes on the thrust panels with high-stiffness beam elements.

Load Simulation

A primary goal of the SLWT LO₂ tank study presented herein is to determine how much additional load, beyond the operational loads, that the tank can withstand before buckling or exhibiting severe bending gradients that will damage the thermal protection system. The basic approach used in the present study to achieve this goal is to apply all of the loads illustrated in Fig. 4 to the model, except for the SRB interface loads. The nodes on the ends of the SRB beam, where the SRB forces act, are restrained so that the SRB interface forces become reactions and rigid body motion is eliminated. Next, the applied loads are separated into two groups. The first group contains the LH₂ tank interface force and moment which are treated in the present study as the primary source of destabilizing compressive stresses in the LO₂ tank that may occur at load levels greater than the corresponding operational load level. The second group of loads consists of the LO₂ pressure (for the second loading condition), the wind load, the structural weight, the thermal load, and the weight of the slosh baffle that is located inside the barrel section of the LO₂ tank. The loads in the second group are constant in value, are part of the operational loads, and are considered to be passive loads when determining the stability margin of safety of the LO₂ tank.

The simple LO₂ pressure distribution and the temperature distribution are input into the STAGS model using the user-written FORTRAN subroutines UPRESS and TEMP, respectively. The wind load is substantially more complicated and required the construction of a Fourier series representation of the pressure field that is input directly into subroutine UPRESS. The slosh baffle weight of approximately 455 lbs is applied to the slosh baffle support rings at XT = 744.85 and XT = 851.0 (see Fig. 2) as eccentric, uniformly distributed line loads. The LH₂ tank interface force and moment are applied to the model

using the least squares loading and moving plane boundary features of STAGS. The least squares loading feature of STAGS permits concentrated forces and moments applied at an axial location to be converted into statically equivalent shell-wall stress resultants using a least squares fit. The moving plane boundary feature of STAGS enforces the geometric constraint that all nodes within the given plane remain coplanar during deformation.

In performing linear bifurcation buckling and nonlinear analyses with STAGS, two load factors, p_a and p_b , are assigned to the first (active) and second (passive) load groups, respectively. First, a linear analysis was conducted to verify that the SRB reactions calculated from the applied loads are reasonably close to the specified values defined previously herein. For both prelaunch loading conditions, the i and k components of the reactions are in good agreement with the corresponding specified values. In contrast, the j components of the reactions were not in very good agreement with the specified values. However, since the j components of the reactions act along the axis of the SRB beam, their effect is mostly contained within the Intertank. As a result, the SRB beam reactions are reasonable approximations to the actual forces.

For the linear bifurcation buckling analyses, the load factor for the passive load group is assigned a value of one ($p_b = 1$) and the load factor for the active load group p_a is defined as the eigenvalue. This approach provides a linear prebuckling stress state in the model that is used in determining the eigenvalue. For the nonlinear analyses, the load factors for both load groups are increased simultaneously to a value of one ($p_a = p_b = 1$) which corresponds to the operational values of the loads and provides the proper nonlinear prebuckling state for the LO₂ tank. Then, the load factor p_a of the primary destabilizing loads is increased until an instability is reached.

Results for SLWT Prelaunch Loads

Results are presented in this section for the two prelaunch loading conditions previously discussed herein. First, results are presented for the loading condition that has a full LH₂ tank and an empty LO₂ tank. Then, results are presented for the loading condition that has a full LH₂ tank and a full LO₂ tank. For this second loading condition, results are presented that were obtained from STAGS models that neglect the slosh baffle ring stiffnesses. Other results were obtained from models that include these ring stiffnesses. These results show that neglecting the slosh baffle ring stiffnesses in the STAGS models yields similar structural deformations and conservative predictions of

the LO₂ tank load carrying capacity at load levels greater than the level of the operational loads.

Full LH₂ and Empty LO₂ Tanks

Several different finite element meshes were used in the present study for the analysis of the LO₂ tank subjected to the prelaunch loading condition with a full LH₂ tank and an empty LO₂ tank. As a first step toward identifying an adequate mesh with as few degrees of freedom as possible, linear bifurcation buckling analyses were conducted. The passive loads associated with load factor p_b were applied to the STAGS models as a linear prebuckling stress state ($p_b = 1$) and the active (destabilizing) loads associated with load factor p_a were used to obtain the minimum eigenvalue.

The meshes investigated in the present study range from 104,600 to 213,500 degrees of freedom. The mesh that was identified as adequate for predicting the linear bifurcation buckling behavior is shown in Fig. 6 and corresponds to 146,700 degrees of freedom. This figure shows a buckle in the LO₂ barrel on the negative Y-axis side of the tank. The reduction in mesh size from 213,500 to 146,700 degrees of freedom was done by increasing the mesh fineness in the local region containing the buckle shown in Fig. 6 and then by eliminating unneeded mesh refinement elsewhere, being careful not to introduce spurious solutions. This step was facilitated by the use of the five-node and seven-node rectangular transition elements available in STAGS. The 104,600 and 146,700 degree-of-freedom models have the same general mesh arrangement shown in Fig. 6, but the level of local refinement of the mesh shown in Fig. 6 for the 146,700 degree-of-freedom model is essentially twice that of the 104,600 degree-of-freedom model. The eigenvalues for the 104,600 and 146,700 degree-of-freedom models are given by $p_a = 3.36$ and $p_a = 3.26$, respectively. These values correspond to loads that are approximately three times the magnitude of the operational loads. Based on the smoothness of the buckling mode shown in Fig. 6 and the three percent difference in the eigenvalues, the 146,700 degree-of-freedom model is considered herein to be adequate for representing the linear bifurcation behavior of the LO₂ tank for this loading condition.

Next, nonlinear analyses of a geometrically imperfect shell were conducted using the 104,600 and 146,700 degree-of-freedom models. An imperfection shape in the form of the corresponding linear bifurcation buckling mode and a negative value of the imperfection-amplitude-to-wall-thickness ratio $A/t = 0.25$ was used in these analyses. The thickness t in the ratio A/t is the minimum-gage wall thickness for the LO₂ barrel and has a value equal to 0.140 in. In

general, the sign of the linear bifurcation buckling mode is arbitrary, and is determined by the specific algorithm used to perform the calculations. For a shell structure with nonnegative Gaussian curvature, the sign of the eigenvector of the buckling mode indicates whether a specific region of the buckling mode of a curved surface is directed toward or away from the concave side of the surface. As a result, these two orientations of the same buckling mode generally correspond to different degrees of nonlinear interaction between imperfection shape and membrane compressive stresses. In the present study, the negative of the linear bifurcation buckling mode amplitude obtained from the STAGS models was used with the imperfection shape because it was found to provide the strongest nonlinear interaction with the compressive stresses in the shell wall. The results of these analyses are shown in Fig. 7 and are presented as a plot of load factor p_a versus the normal displacement of the shell wall at the largest crest of the buckle defined by the coordinates $XT = 787.97$ and $\theta = 300.94$ degrees (see Fig. 2 for coordinate definitions). The dashed and solid lines shown in the figure correspond to the 104,600 degree-of-freedom and 146,700 degree-of-freedom models, respectively. The unfilled square symbols and the filled circular symbols shown in the figure correspond to the actual analytical results obtained for the 104,600 degree-of-freedom and 146,700 degree-of-freedom models, respectively. The results shown in Fig. 7 indicate that there is a small discrepancy between the two nonlinear solutions. The solution for the more refined model has larger values of displacements for some values of the load factor. This discrepancy is attributed to the fact that the less refined model overestimates the bending stiffness of the shell wall. The results in Fig. 7 also suggest that the 146,700 degree-of-freedom model is adequate for conducting nonlinear analyses for this loading condition.

Results obtained from nonlinear analyses for a geometrically perfect shell and for geometrically imperfect shells with values for the imperfection-amplitude-to-wall-thickness ratio $A/t = 0.25, 0.5$, and 1.0 are presented in Fig. 8. These results were obtained using the 146,700 degree-of-freedom model and with the imperfection shape in the form of the corresponding linear bifurcation buckling mode with a negative amplitude. The filled circles in the figure indicate solutions for the geometrically perfect shell, and the unfilled squares, triangles, and circles indicate solutions for the geometrically imperfect shells with $A/t = 0.25, 0.5$, and 1.0 , respectively. The horizontal dashed line shown in the figure represents the linear bifurcation buckling load level. The results shown in Fig. 8 are presented as a plot of the load factor p_a versus the normal displacement of the shell wall at the largest crest of the buckle defined by the coordinates $XT = 789.939$ and $\theta = 301.64$ degrees. These results indicate that the

barrel section of the LO₂ tank, where the buckles appear, exhibits stable postbuckling load carrying capacity for the geometrically imperfect shells and, as a result, is insensitive to initial imperfections. Moreover, the shallowness of the barrel panel containing the buckle and the presence of stable postbuckling load carrying capacity suggest that the buckling behavior is essentially that of the stable-symmetric bifurcation type; that is, the unstable-asymmetric bifurcation behavior usually associated with singly curved panels is essentially benign.

The buckle patterns obtained from the linear bifurcation analysis and the nonlinear analyses are all very similar in shape and occur in the same location. The stress distribution in the shell that causes the buckle pattern to form is shown in Fig. 9 for a geometrically perfect shell and for $p_a = p_b = 1$. Contours of the membrane meridional and shear stresses on the negative Y-axis side ($\theta = 270$ degrees) of the tank are shown in Figs. 9a and 9b, respectively, and are given in units of psi. These contours indicate that high meridional compression stresses exist above the thrust panel as expected. The contours also indicate that buckling occurs in a region of the barrel where there are significant shear stresses in the shell which interact with the meridional compressive stresses and reduce the buckling load.

Full LH₂ and LO₂ Tanks

Several different finite element meshes were also used in the present study for the analysis of the LO₂ tank subjected to the prelaunch loading condition with full LH₂ and LO₂ tanks. Linear bifurcation buckling analyses were conducted first to identify an adequate mesh for modeling the behavior of the shell with as few degrees of freedom as possible. The passive loads associated with load factor p_b were applied to the STAGS models as a linear prebuckling stress state ($p_b = 1$) and the active (destabilizing) loads associated with load factor p_a were used to obtain the minimum eigenvalue.

The meshes investigated for this prelaunch loading condition range from 48,990 to 121,500 degrees of freedom. The mesh that was identified as being adequate for predicting linear bifurcation buckling is shown in Fig. 10 and corresponds to 99,100 degrees of freedom. The reduction in mesh size from 121,500 to 99,100 degrees of freedom was achieved by increasing the mesh in the region surrounding the buckle, and then by eliminating unneeded mesh refinement elsewhere in a manner similar to that used for the previous loading condition. A 79,950 degree-of-freedom model was investigated that has the same general mesh arrangement shown in Fig. 10, but with the local refinement shown

on the right-hand-side of the ogive used for both locally refined regions of the ogive. The eigenvalues for the 79,950 and 99,100 degree-of-freedom models are given by $p_a = 3.94$ and $p_a = 3.78$, respectively, where a value of 1.0 corresponds to the magnitude of the operational loads. Because of the smoothness of the buckling mode shown in Fig. 10 and the 4 percent difference in the eigenvalues, the 99,100 degree-of-freedom model is used herein to represent the linear bifurcation behavior of the LO₂ tank for this loading condition. Nonlinear solutions were also obtained for a geometrically perfect shell using the 79,950 and 99,100 degree-of-freedom models. These solutions are in excellent agreement and indicate that the 99,100 degree-of-freedom model is adequate for representing the nonlinear behavior of the LO₂ tank for this loading condition. Thus, all subsequent results presented in this section of the present paper were obtained using the 99,100 degree-of-freedom model.

A short-wavelength buckle in the forward part of the aft ogive is shown in Fig. 10 that is essentially a wrinkle in the skin on the negative Y-axis side of the tank. The loads acting along the shell meridians near the SRB attachment point develop the meridional compressive stress resultants shown in Fig. 11a (given in lbs/in. for $p_a = p_b = 1$) that cause the buckling mode shown in Fig. 10. Insight into the formation of the buckling mode is obtained by noting that Gaussian curvature is a geometric measure that is related to how much the shell membrane stiffness participates in its bending deformations. The results in Fig. 11 indicate that the meridional compressive stress resultants and the circumferential tension stress resultants increase in the LO₂ tank from the tip of the forward ogive to the Intertank. The magnitude of the shell Gaussian curvature decreases in this part of the shell which causes local buckling to occur at this location. In the forward ogive, there are relatively small values of hoop tensile stresses to stabilize the shell, but the Gaussian curvature is high. In the aft ogive, the meridional compressive stresses and hoop tensile stresses are larger than in the forward ogive, but the Gaussian curvature is much smaller. The STAGS results suggest that the higher values of meridional compressive stresses and lower values of Gaussian curvature in the aft ogive are the dominant factors that influence the location of the buckling mode. These results also indicate that the shortness of the half-wave length of the buckling mode is a result of the high values of the circumferential tensile stress resultants shown in Fig. 11 that are caused by the hydrostatic pressure exerted on the shell wall by the LO₂.

Results obtained from nonlinear analyses of a geometrically perfect shell and a geometrically imperfect shell with an imperfection-amplitude-to-wall-thickness ratio $A/t = 0.3$ are presented in Fig. 12 and 13,

respectively. The thickness t in the ratio A/t is the minimum-gage wall thickness of the aft ogive and has a value equal to 0.100 in. The results shown in Fig. 13 were obtained using an imperfection shape that is in the form of the corresponding linear bifurcation buckling mode with a negative amplitude. The negative of the linear bifurcation buckling mode amplitude obtained was used as the imperfection shape because it provided the strongest nonlinear interaction with the compressive stresses in the shell wall. The results shown in these two figures are for nonlinear solutions that were obtained by increasing the load factors p_a and p_b simultaneously to a value of one, and then holding p_b constant while increasing the magnitude of the load factor p_a . The normal displacements along the length of the aft ogive shell wall are represented by the solid lines in the figures for values of the load factor p_a approximately equal to 3.0, 4.0, and 5.0. The linear bifurcation mode is represented by the dashed line in the figures with normalized amplitudes given by the right-hand ordinate of the figures. The bifurcation mode in the figures indicates how the imperfection shape influences the nonlinear solution. The solid lines shown in the figures predict a short-wave-length bending response in the aft ogive over the negative Y-axis ($\theta = 270$ degrees) that is similar in shape to the corresponding linear bifurcation buckling mode shape. The overall slope of the solid lines (obtained by fitting a straight line to each curve) in the figures is due to the outward displacement of the shell wall caused by the increase in pressure as p_a and p_b are simultaneously increased to a value of one in the nonlinear analysis. This effect is not represented in the linear prebuckling stress state used in a linear bifurcation buckling analysis and, as a result, does not affect the overall slope of the dashed lines.

The results presented in Figs. 12 and 13 predict a stable nonlinear response at load levels greater than the load predicted by the linear bifurcation buckling analysis ($p_a = 3.78$). As the load increases, substantial bending gradients (indicated by the waviness of the curves) develop and grow in the shell wall which reduce the apparent meridional stiffness of the aft ogive. The nonuniformity of the bending gradients is due to the thickness variations in the ogive and the presence of the weld lands. These results indicate that a geometrical imperfection in the shape of the linear bifurcation buckling mode and with a small negative amplitude will greatly increase the severity of the bending gradients and will cause the growth of the bending gradients to start at much lower load levels.

The reduction in apparent meridional stiffness of the aft ogive is shown more explicitly in Fig. 14. In this figure, the intensities of the bending gradients (indicated by the magnitude of the normal displacement amplitude) at $XT = 637.66$ for the geometrically perfect

shell (see $x = 99.3$ in Fig. 12) and at $XT = 633.77$ for the geometrically imperfect shell (see $x = 95.4$ in Fig. 13) are given as a function of the load factor p_a . These locations represent the locations of the largest bending gradients shown in Figs. 12 and 13. The amplitude Δw shown in Fig. 14 is the distance from the maximum value of the local shell-wall displacement to the adjacent minimum value and represents the intensity of the local bending gradient in the response. The filled circles shown in the figure correspond to results for a geometrically perfect shell and the unfilled triangles and squares correspond to results for geometrically imperfect shells with imperfection-amplitude-to-wall-thickness ratios of $A/t = 0.1$ and 0.3 , respectively ($t = 0.100$ in.). The horizontal dashed line shown in the figure represents the linear bifurcation buckling load level.

The results shown in Fig. 14 indicate that the amplitude of the greatest local bending gradient grows with increasing load, and that the amount of growth increases substantially with increasing geometric imperfection amplitude. The results predict that the shell can support loads greater than the critical buckling load predicted by a linear bifurcation buckling analysis. As Δw increases, the apparent meridional stiffness decreases, and as a result, the positive-valued constant of proportionality between an increment in load and the corresponding increment in displacement amplitude decreases. This trend is manifested by the reduction in slope of the load versus displacement amplitude curves. This type of response is similar to the response reported by Stevens, Starnes, and Almroth in Ref. 2 for cylindrical shells subjected to combined internal pressure and a pure bending moment. The results in Ref. 2 indicate that the amplitude of the short-wave-length deflection approaches a horizontal tangent as the load increases, and that the value of the load for the horizontal tangent corresponds to a local collapse mode of the cylinder. Mathematically, the horizontal tangent indicates that unbounded growth of the displacement occurs for an infinitesimal increase in the load. It is expected that the curves shown in Fig. 14 would approach a horizontal tangent as Δw increases until a redistribution in load occurs within the aft ogive. As a horizontal tangent in a load versus displacement amplitude curve is approached, the region of the shell containing the bending gradients becomes incapable of supporting additional load and the compressive load is redistributed to another portion of the aft ogive. If other parts of the ogive are incapable of supporting the compressive load, the shell will collapse. However, if other parts of the ogive are capable of supporting the compressive load, the slope of the load versus displacement amplitude curve will increase as the loading increases. Geometric imperfections with large amplitudes can also cause a similar redistribution in load and, as a result, the corresponding slope of the load versus displacement amplitude curve would increase.

Similar curves for smaller geometric imperfection amplitudes would approach a horizontal tangent.

The results presented in Figs. 12 through 14 indicate that large local bending gradients may occur in the shell wall for loads that are much smaller than the local collapse load and may cause the thermal protection system (TPS) to disbond from the shell wall and fail. The results presented in Fig. 15 indicate approximate estimates of the local radius of curvature for the largest bending gradient appearing in the aft ogive along the negative Y-axis ($\theta = 270$ degrees). These bending gradients are located at $XT = 637.66$ for the geometrically perfect shell (see $x = 99.3$ in Fig. 12) and at $XT = 633.77$ for the geometrically imperfect shells (see $x = 95.4$ in Fig. 13). The local radius of curvature ρ shown in the right-hand sketch of the figure is calculated by the formula

$$\rho = \frac{[1 + (w')^2]^{3/2}}{|w''|}$$

where w' is the local displacement shown in the right-hand sketch in Fig. 15 and is approximated by $w' = \frac{\Delta w}{2} \sin \frac{2\pi x}{\lambda}$ where λ is the buckle wave length.

At the crests of the wave defined by $x = \lambda/4$ and $3\lambda/4$, $w' = 0$, and the radius of curvature is given by $\rho = \frac{\lambda^2}{2\pi^2 \Delta w}$. The filled circles shown in the figure correspond to results for the geometrically perfect shell, and the unfilled triangles and squares correspond to results for geometrically imperfect shells with imperfection-amplitude-to-wall-thickness ratios of $A/t = 0.1$ and 0.3 , respectively. The imperfection shape is identical to the linear bifurcation buckling mode with a negative amplitude shown in Fig. 13. The results in Fig. 15 demonstrate that the geometric imperfection amplitude has a significant influence on the local radius of curvature of the shell wall. For example, if a given thermal protection system is known to disbond from the shell wall at a value of $\rho = 100$ in., the maximum load factor is reduced from a value of approximately 4.8 for the geometrically perfect shell to 3.2 for the geometrically imperfect shell with $A/t = 0.3$.

Results for SWT Full-Scale Structural Tests

To assess the accuracy of the STAGS model of the SLWT LO₂ tank, finite element analyses were performed on two full-scale structural tests using the same modeling approach described previously in the present paper. The two full-scale tests were conducted at the NASA George C. Marshall Spaceflight Center on the original standard-weight ET (SWT) during the

development program of the original Space Shuttle ET. Precise measurements of initial geometric imperfections in the tank wall were not made for either of these test specimens. As a result, these test results can only be used as a qualitative means for assessing the accuracy of the STAGS model of the SLWT LO₂ tank.

The SWT LO₂ tank has essentially the same geometry as the SLWT LO₂ tank, but is made of 2219 aluminum alloy. The primary difference between the two LO₂ tanks is that the skins of the SWT are thicker than those of the SLWT, and the thicknesses are much more uniformly distributed over the SWT shell. Thus, the modeling approach previously described herein for the SLWT is used to model the two full-scale SWT test articles. The SWT model was generated by modifying the STAGS user-written subroutine WALL for the SLWT to account for the SWT thicknesses. The differences between the SWT Intertank and the SLWT Intertank are negligible for the purposes of transferring loads from the Intertank to the LO₂ tank. The two full-scale SWT tests described subsequently are referred to herein as the structural test article (STA) and the ground vibration test article (GVTA).

Results for the STA

The STA consisted of a SWT LO₂ tank and a SWT Intertank mounted vertically to a LH₂ tank load simulator and to two rigid vertical posts at the SRB attachment points. The LH₂ tank load simulator is modeled herein by a self-equilibrated line load applied to the bottom of the Intertank as indicated in Fig. 16. A uniformly distributed circumferential line load of 1,394 kips was also applied to the tank at $XT = 852.8$. For the test, these two loads were applied and then the tank was filled with room temperature water while maintaining an ullage pressure in the tank. After filling the tank to $XT = 455$, a depth of approximately 42 feet, the ullage pressure was slowly reduced. When the ullage pressure reached 0.57 psig, the tank unexpectedly buckled in the forward ogive between $XT = 455$ and $XT = 475$ and between $\theta = 253$ and 277 degrees (negative Y-axis side of the tank). The SRB interface forces reacted at the two vertical posts had magnitudes equal to 1,295 kips and are shown in Fig. 16.

To simulate the test loading conditions in a practical manner, all loads shown in Fig. 16, except for the SRB beam loads, are controlled by the load factor p_a . A value of $p_a = 1$ corresponds to values of the loads at which the actual test article buckled. The loads at the ends of the SRB beam are computed as reactions and have been found to be in excellent agreement with the corresponding SRB beam loads shown in Fig. 16.

Finite element meshes were constructed for the STA and a limited convergence study was performed following an approach similar to that described herein for the SLWT analyses. The final mesh used to analyze the STA has 159,993 degrees of freedom and is highly refined in the forward ogive on the negative Y-axis side of the tank. The linear bifurcation buckling mode obtained for the STA using this mesh is shown in Fig. 17. This buckling mode is a short-wavelength buckle similar to the one obtained for the SLWT prelaunch loading condition with full LH₂ and LO₂ tanks. The location of the buckling mode shown in this figure is the same as the location observed during the test. The eigenvalue is given by $p_a = 1.14$.

Next, a series of nonlinear analyses were conducted using the 159,993 degree-of-freedom mesh for values of the imperfection-amplitude-to-wall-thickness ratio $A/t = 0, 0.1, 0.25, 0.5$, and 1.0 . The thickness t in the ratio A/t is the minimum-gage wall thickness of the forward ogive and has a value equal to 0.080 in. For each of these cases, the geometric imperfection shape is input in the form of the linear bifurcation buckling mode shown in Fig. 17 with a negative amplitude to obtain the strongest interaction between the membrane compressive stress and shell wall deformations.

The results of the nonlinear analyses of the STA are shown in Fig. 18. The maximum normal displacement that occurs at the crest of the buckle pattern is shown in the figure as a function of the load factor p_a . The buckle crest is located at $XT = 457.6$ and $XT = 466.6$ for the geometrically perfect and imperfect shells, respectively, and at $\theta = 267.2$ degrees. The filled circles and the unfilled circles, diamonds, squares, and triangles correspond to results for $A/t = 0, 0.1, 0.25, 0.5$, and 1.0 , respectively. The results for all values of A/t indicate a monotonic increase in load with increasing normal displacement. However, a maximum load is reached at which numerical difficulties were encountered in the nonlinear solutions. After several unsuccessful tries to increase the load above these values, it was concluded that the last data point on each curve corresponds to a limit point of the shell response. At each limit point, the shell buckled into a mode similar in shape to the buckling mode shown in Fig. 17 and at the same location. The meridional and circumferential stress resultant distributions are similar to those presented in Fig. 11 for the prelaunch loading condition with full LH₂ and LO₂ tanks.

The values of the limit points are shown in Fig. 19 as a function of geometric imperfection amplitude and load factor, and indicate the imperfection sensitivity of the STA. The limit points obtained for the STA span a broad load range bounded by $p_a = 1.18$ for a geometrically perfect shell and $p_a = 0.53$ for a geometrically imperfect shell with $A/t = 1.0$ ($A =$

0.080 in.). This load range corresponds to a 55 percent reduction in load carrying capacity of a geometrically perfect shell. The dashed line shown in the figure has a value of $A/t = 0.064$ for $p_a = 1$ (which corresponds to the buckling load of the test). This result suggests that the STAGS modeling approach described herein provides a reasonably accurate indication of the SWT behavior. Because of the similar geometric character of the SWT and the SLWT, the results also suggest that the SLWT model described herein should provide a reasonable representation of the SLWT nonlinear shell response.

Results for the GVTA

The GVTA consisted of a SWT mounted on two Solid Rocket Boosters and an Orbiter attached to the SWT. The SWT consisted of a LO₂ tank, a LH₂ tank, and an Intertank. In this configuration, the SWT is inclined at an angle of approximately 10 degrees in the XT-Z plane because of the eccentric weight of the Orbiter. The loads acting on the LO₂ tank and Intertank during the test and the inclination angle α are shown in Fig. 20. These loads consist of two SRB interface force components, the LH₂ tank interface force and moment, a uniformly distributed circumferential line load of 20.86 kips that is applied at $XT = 852.8$, and a hydrostatic water pressure distribution corresponding to the tank fill level of $XT = 645$ (a depth of approximately 26.5 feet). No ullage pressure was present inside the LO₂ tank during the test. The hydrostatic pressure distribution for the GVTA is defined in the STAGS model with user-written subroutine UPRESS in terms of the local axial coordinate x shown in Fig. 20b. The pressure distribution is given by $p(x,\theta) = 0$ for values of $x \leq x_f - r(x) \tan\alpha \cos\theta$, where x_f is the local coordinate of the fill level that is defined by the positive numerical difference between stations $XT = 645$ and $XT = 371$, as shown in Fig. 20b. The symbol θ is the cylindrical coordinate defined in Fig. 2, and $r(x)$ is the polar radius of the shell reference surface (see Fig. 20b) that is calculated from the differential geometry of the LO₂ tank components. For the remaining values of x , the pressure is given by

$$p(x,\theta) = \gamma \left[(x - x_f) \cos\alpha + r(x) \sin\alpha \cos\theta \right]$$

where γ is the specific weight of water at room temperature.

The original test plan for the GVTA was to fill the tank with water and then to perform a ground vibration test. However, when the water fill level reached $XT = 645$, the tank unexpectedly buckled in the forward ogive between approximately $XT = 437$ and $XT = 503$ and

between $\theta = 247$ and 281 degrees (negative Y-axis side of the tank).

The test loading conditions for the GVTA are simulated in the manner described herein for the STA; that is, all loads shown in Fig. 20, except for the SRB interface forces, are assigned to the load factor p_a such that a value of $p_a = 1$ corresponds to buckling of the test article. The loads at the ends of the SRB beam are computed as reactions and have been found to be in excellent agreement with the SRB interface forces shown in Fig. 20a.

Several finite element meshes were also investigated for the GVTA following the same approach used for the STA. The final mesh selected to analyze the GVTA has 252,300 degrees of freedom and is highly refined in the forward ogive on the negative Y-axis side of the tank. The linear bifurcation buckling mode obtained for the GVTA using this mesh is shown in Fig. 21. This buckling mode is also a short-wavelength buckling mode similar to the one obtained for the SLWT prelaunch loading condition with full LH₂ and LO₂ tanks and for the STA. The location of the buckling mode shown in this figure is essentially the same as the location observed during the test. The eigenvalue is given by $p_a = 2.41$.

Next, nonlinear analyses were conducted using the 252,300 degree-of-freedom mesh for values of the imperfection-amplitude-to-wall-thickness ratio $A/t = 0, 0.125, 0.25, 0.5, 0.75$, and 1.0 . The minimum-gage wall thickness t for the forward ogive has a value equal to 0.080 in. For each of these cases, the geometric imperfection shape was in the form of the linear bifurcation buckling mode shown in Fig. 21 with a negative amplitude.

The results of the nonlinear analyses of the GVTA are shown in Fig. 22. The maximum normal displacement that occurs at the crest of the buckle pattern is located at $XT = 466.7$ and at $\theta = 267.2$ degrees, and is shown in the figure as a function of the load factor p_a . The filled squares, triangles, and circles and the unfilled circles, squares, and triangles correspond to results for $A/t = 0, 0.125, 0.25, 0.5, 0.75$, and 1.0 , respectively. Similar to the STA results, the GVTA results indicate a monotonic increase in load with increasing normal displacement that terminates at a limit point for all values of A/t . At each limit point, the shell buckles into a mode similar in shape to the mode shown in Fig. 21 and at the same location. The values of the limit points are shown in Fig. 23 as a function of the geometric imperfection amplitude and load factor, and indicate the imperfection sensitivity of the GVTA. The limit points obtained for the GVTA span a broad load range bounded by $p_a = 2.46$ for a geometrically perfect shell and $p_a = 0.92$ for a

geometrically imperfect shell with $A/t = 1$. This load range corresponds to a 62 percent reduction in load carrying capacity of a geometrically perfect shell. The load reduction for the GVTA is approximately 7 percent greater than that for the STA. The dashed line shown in Fig. 23 has a value of $A/t = 0.625$ ($A = 0.050$ in.) for $p_a = 1$ (which corresponds to the buckling load of the test). This result also suggests that the STAGS modeling approach described herein provides a reasonably accurate indication of the SWT behavior and the SLWT nonlinear shell response.

Concluding Remarks

The results of buckling and nonlinear analyses of the Space Shuttle super-lightweight tank (SLWT) liquid-oxygen (LO₂) tank have been presented. An overview of the LO₂ tank and Intertank structure, and the loading conditions for two important prelaunch loading conditions have been described. In addition, the analysis code used in the present study has been described and the finite element modeling approach and details have been presented. The analytical method used in the present study to simulate the loading conditions associated with prelaunch fueling of the Space Shuttle has been discussed.

Results have been presented herein for the SLWT LO₂ subjected to two prelaunch loading conditions and for two full-scale structural tests that were conducted during the development program of the original standard-weight tank (SWT). These results illustrate three distinctly different types of nonlinear response for thin-walled shells subjected to combined mechanical and thermal loads that may be encountered in the design of other liquid-fuel launch vehicles. Predicting the response of these shells generally requires large-scale, high-fidelity finite element models to represent the response accurately. For the first SLWT prelaunch loading condition, the liquid-hydrogen (LH₂) tank is full and the LO₂ tank is empty. The analytical results predict that the nonlinear response is characterized by a buckling response that is insensitive to initial geometric imperfections. For this loading condition, the barrel section of the LO₂ tank is predicted to buckle at loads that are more than twice the operational loads. For the second SLWT prelaunch loading condition, the LH₂ and LO₂ tanks are full. The nonlinear response for this loading condition is characterized by a short-wavelength bending gradient that grows in amplitude in a stable manner with increasing load. For this loading condition, local bending gradients appear in the aft ogive of the LO₂ tank that do not lead to a general instability mode, but may cause failure of the thermal protection system for load levels in excess of approximately twice the operational load level. Moreover, the results predict that the severity of the

local gradients is significantly affected by localized initial geometric imperfections.

For the two full-scale structural tests of the SWT, the nonlinear responses exhibit local buckling of a doubly curved shell segment of the LO₂ tank forward ogive that is characterized by a limit-point behavior. The magnitude of the load level corresponding to the limit point has been shown to be very sensitive to local initial geometric imperfections in the LO₂ tank. Specifically, load reductions of about 55 to 62 percent of the buckling load of a geometrically perfect shell are predicted for a geometric imperfection shape in the form of the linear bifurcation buckling mode and with a one-wall-thickness imperfection amplitude. The buckling loads obtained from both tests correspond to geometric imperfection amplitudes that are less than one minimum-gage wall thickness. For both tests, the analytical results suggest that the finite element modeling approach used in the present study represents the nonlinear behavior of the SLWT LO₂ tank very well.

Acknowledgments

The authors would like to express their thanks to Mr. Richard D. Young, Mr. Walter L. Heard, Jr., Dr. Charles C. Rankin, Mr. Michael Quiggle, and Mr. Neil Otte of Lockheed-Martin Engineering and Sciences Services, NASA Langley Research Center (retired), Lockheed-Martin Missiles and Space Company, Lockheed-Martin Manned Space Systems Division, and the NASA George C. Marshall Space Flight Center, respectively, for their technical support.

References

1. Brogan, F. A., Rankin, C. C., and Cabiness, H. D., "STAGS User Manual," Lockheed Palo Alto Research Laboratory, Report LMSC P032594, 1994.
2. Stephens, W. B., Starnes, J. H., Jr., and Almroth, B. O., "Collapse of Long Cylindrical Shells under Combined Bending and Pressure Loads," *AIAA Journal*, Vol. 13, No. 1, January 1975, pp. 20-25.

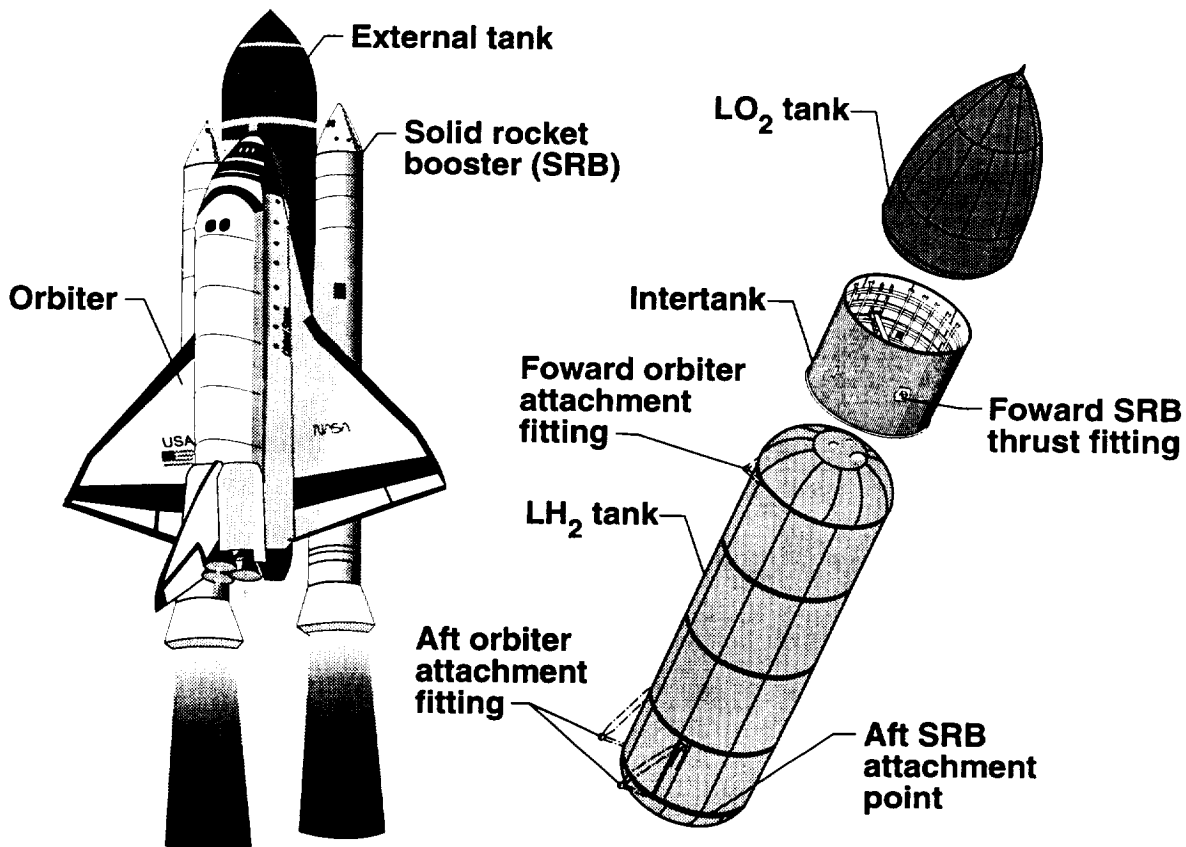


Fig. 1 Space Shuttle External Tank components.

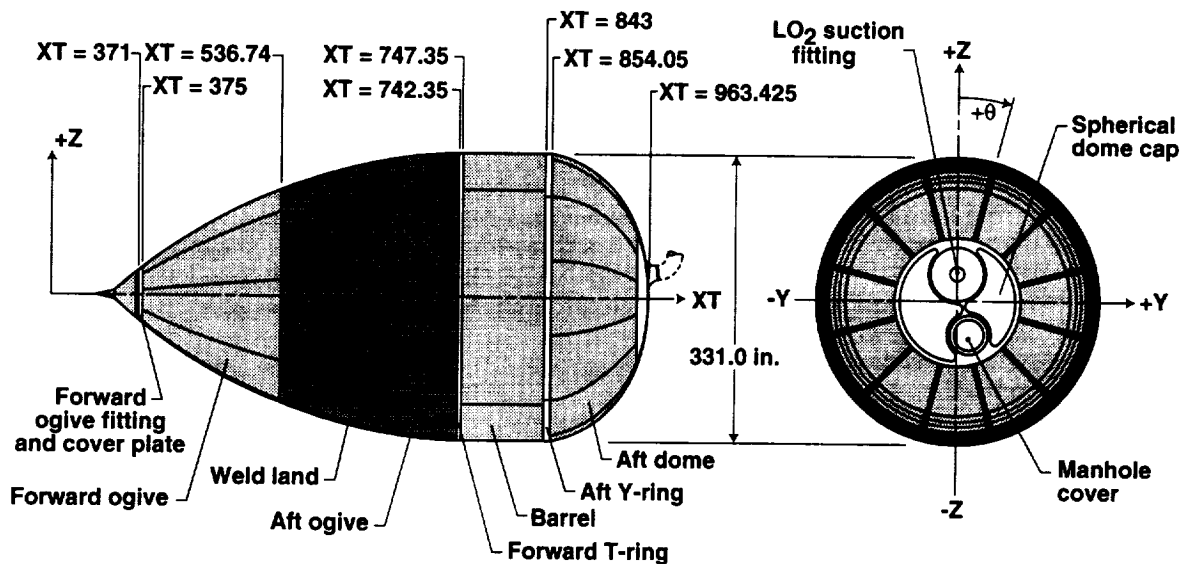


Fig 2. LO₂ tank structural components (values of XT are given in inches).

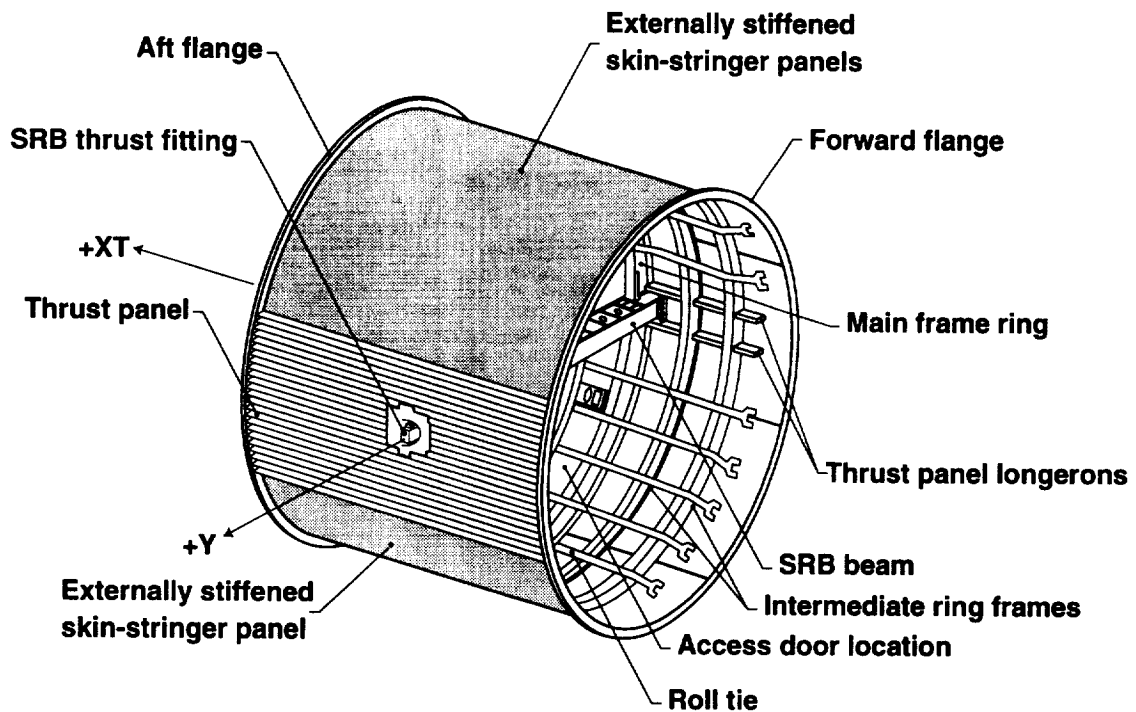


Fig 3. Intertank structure.

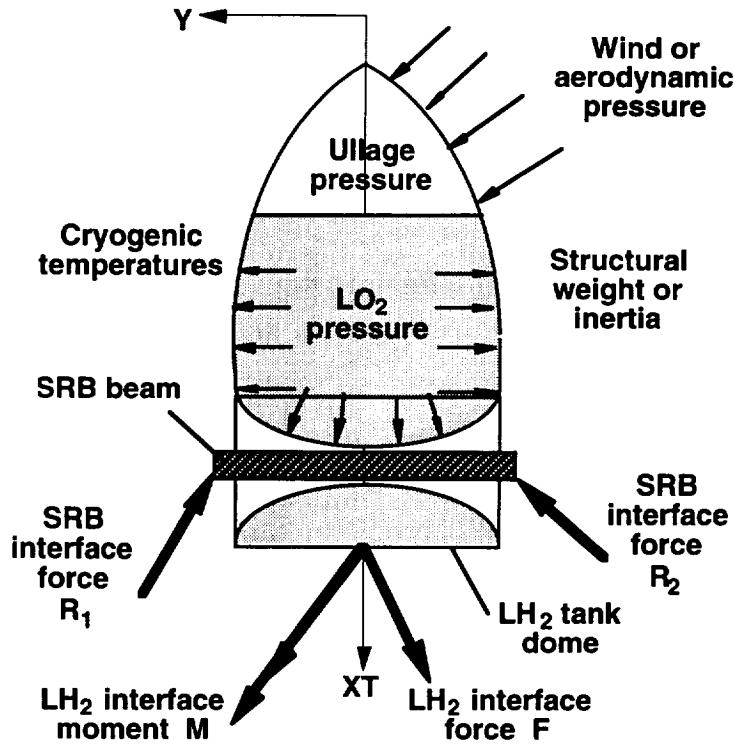


Fig. 4 Loading characteristics.

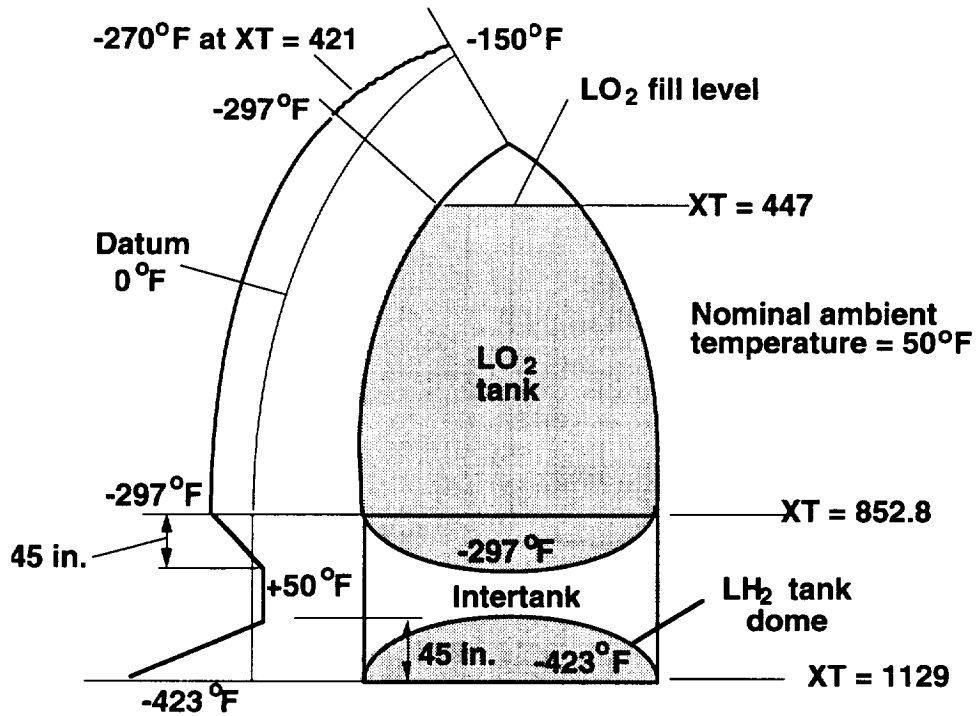


Fig. 5 Axisymmetric temperature profile for prelaunch loading case with full LH₂ and LO₂ tanks.

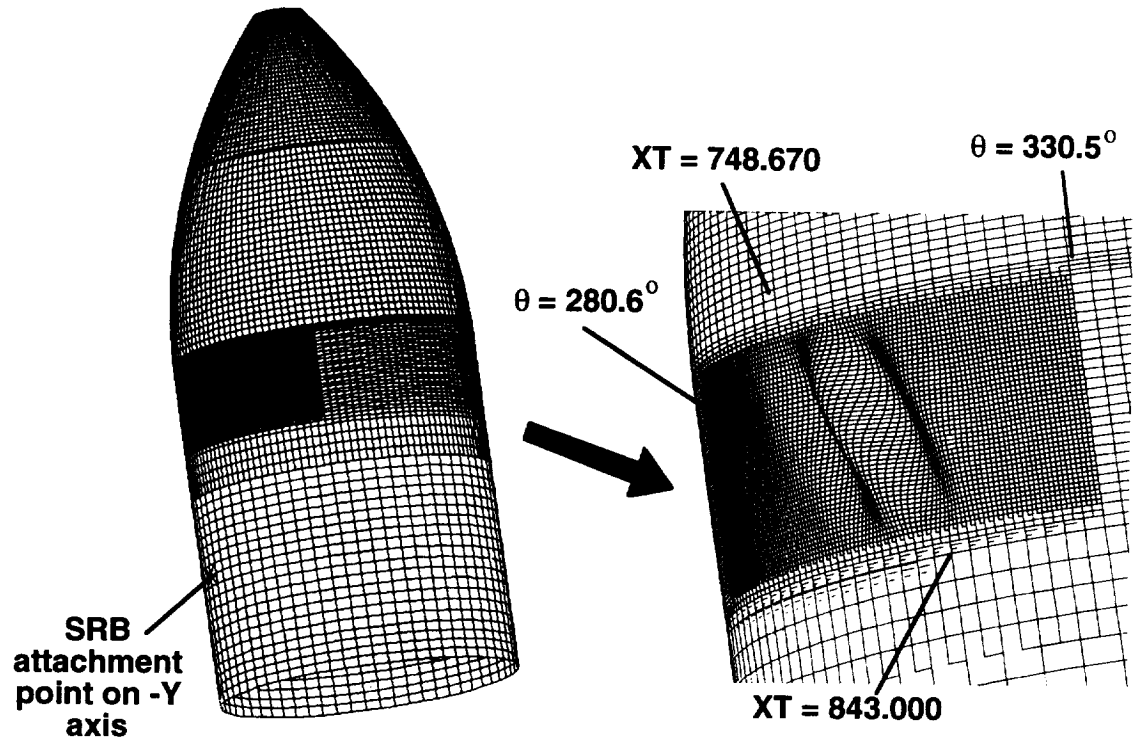


Fig. 6 Linear bifurcation buckling mode for prelaunch loading condition with full LH₂ tank and empty LO₂ tank (146,700 degrees of freedom).

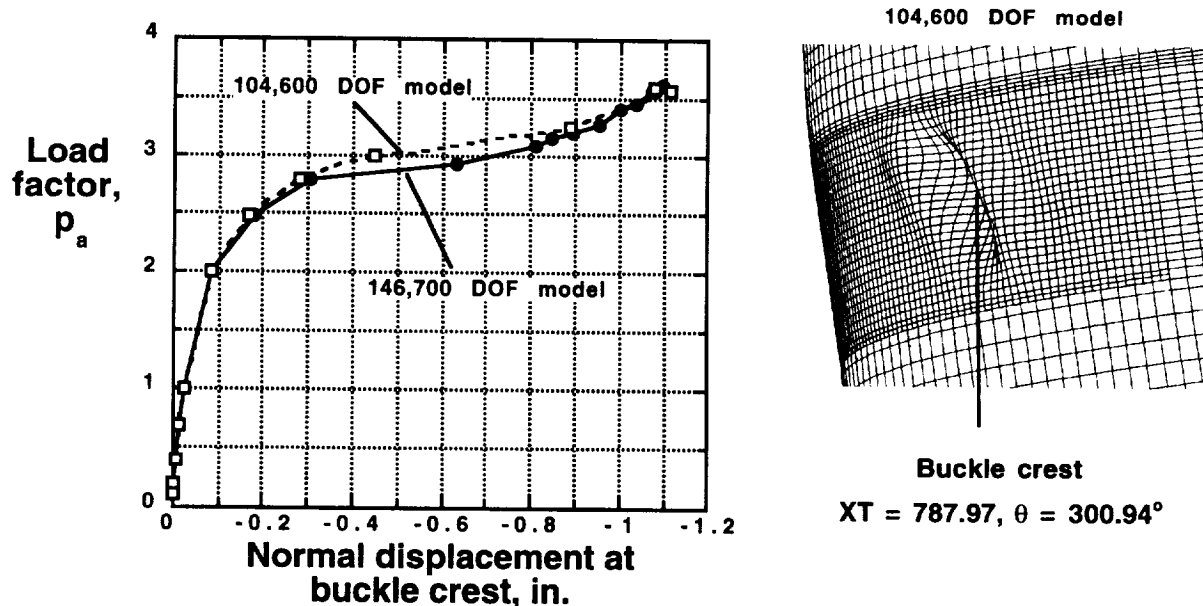


Fig. 7 Convergence of nonlinear solutions for the prelaunch loading condition with full LH₂ and empty LO₂ tanks (imperfection-amplitude-to-shell-thickness ratio A/t = 0.25).

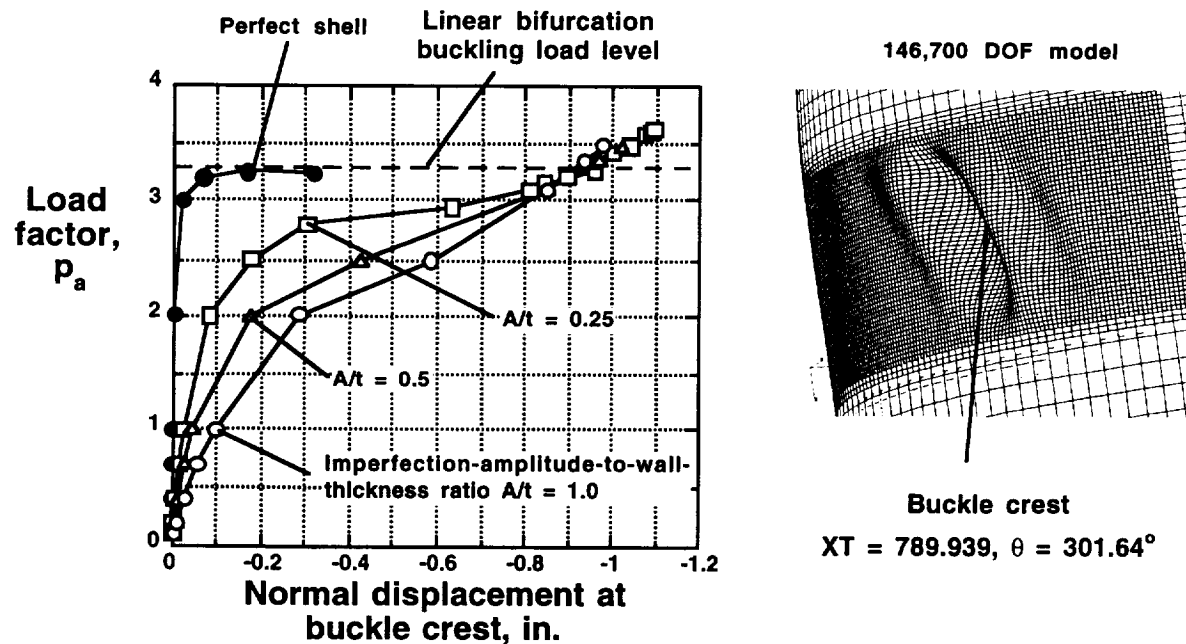


Fig. 8 Effect of imperfection amplitude on the nonlinear solutions for the prelaunch loading condition with full LH₂ and empty LO₂ tanks.

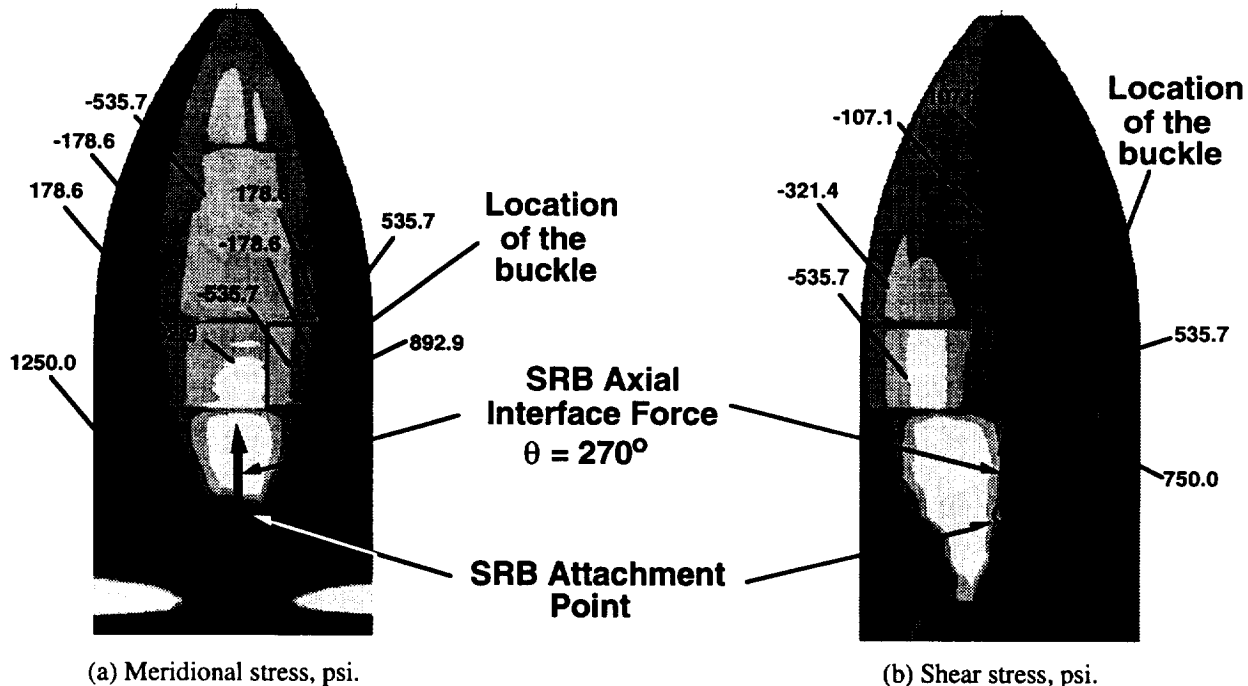


Fig. 9 Membrane stress distributions in geometrically perfect LO₂ tank and Intertank for the loading condition with full LH₂ and empty LO₂ tanks ($p_a = p_b = 1$).

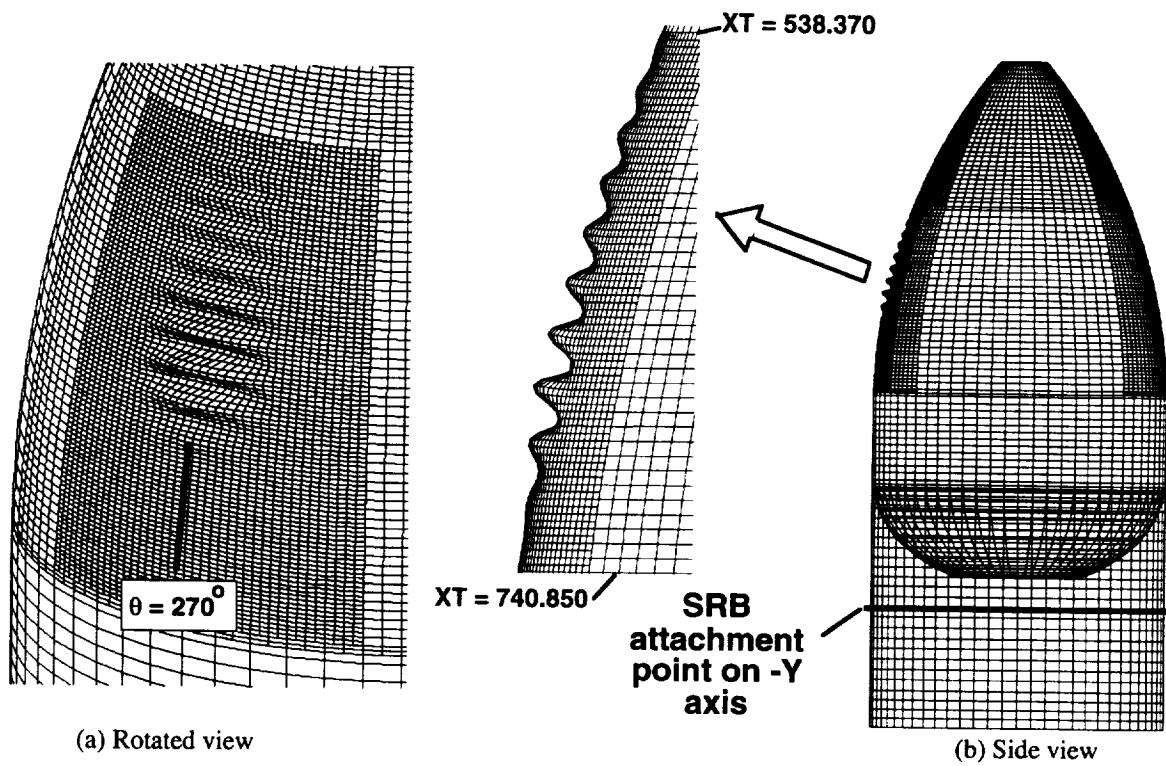


Fig. 10 Linear bifurcation buckling mode for prelaunch loading condition with full LH₂ and LO₂ tanks (99,100 degrees of freedom).

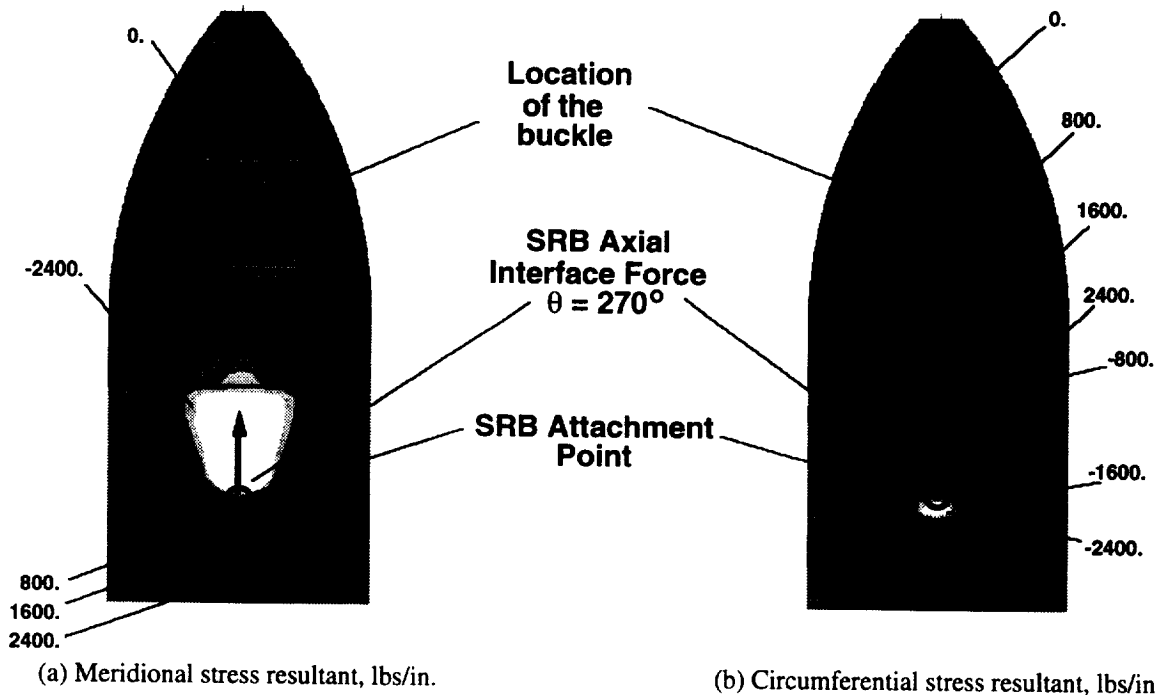


Fig. 11 Stress distributions in the geometrically perfect LO₂ tank and Intertank for the loading condition with full LH₂ and LO₂ tanks ($p_a = p_b = 1$).

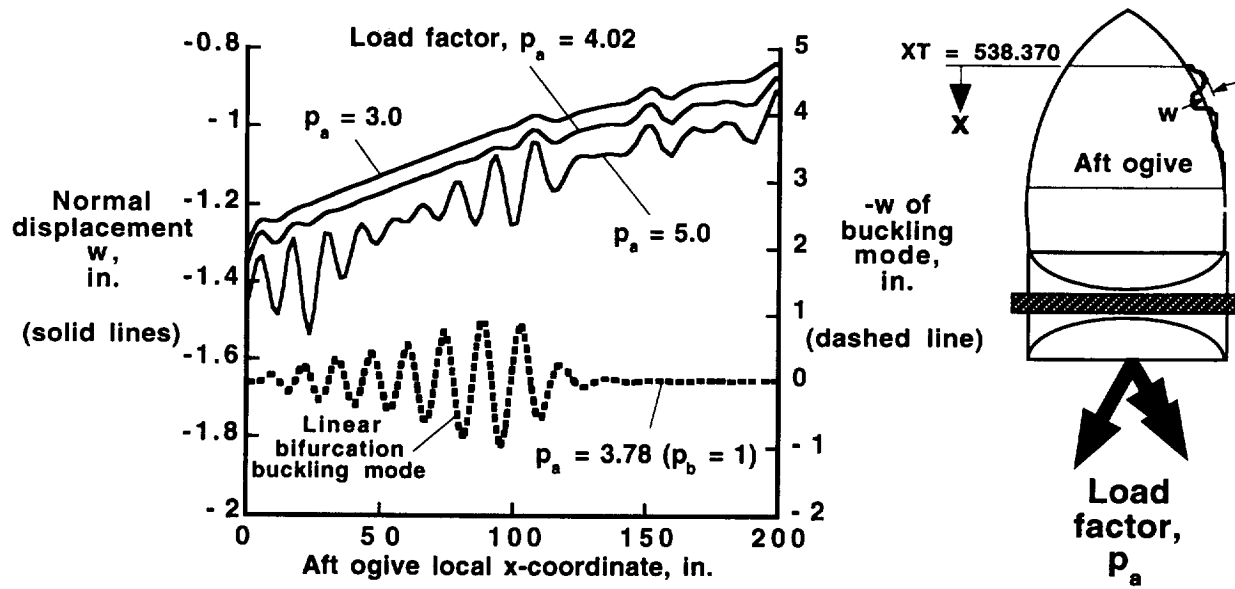


Fig. 12 Bending gradients in the aft ogive of a geometrically perfect LO₂ tank shell for the prelaunch loading condition with full LH₂ and LO₂ tanks ($\theta = 270^\circ$).

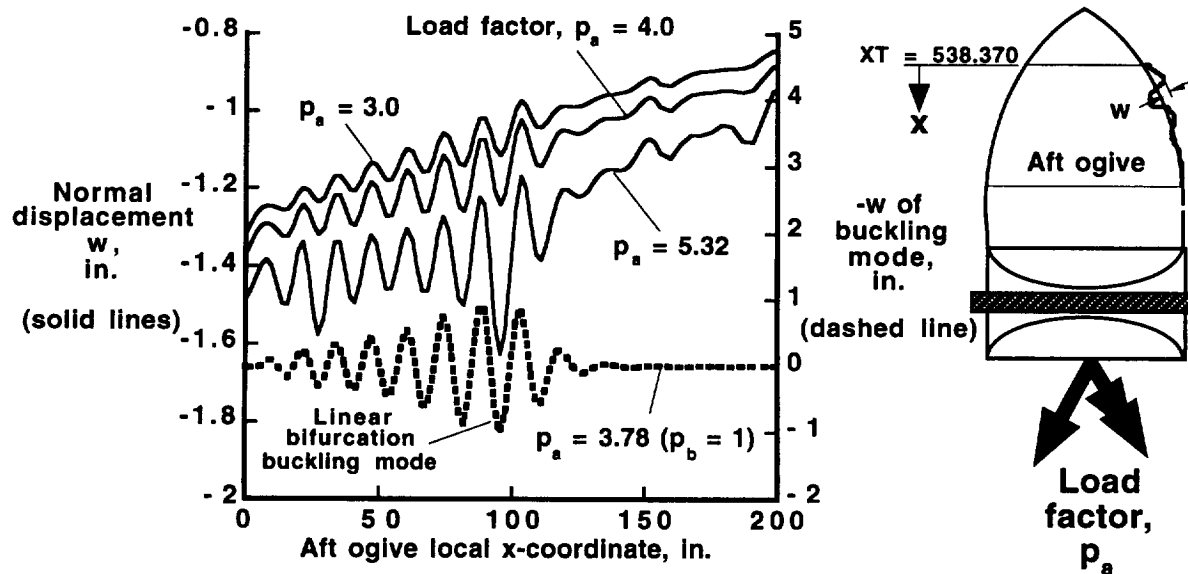


Fig. 13 Bending gradients in the aft ogive of a geometrically imperfect LO₂ tank shell for the prelaunch loading condition with full LH₂ and LO₂ tanks ($\theta = 270^\circ$, imperfection-amplitude-to-wall-thickness ratio $A/t = 0.3$).

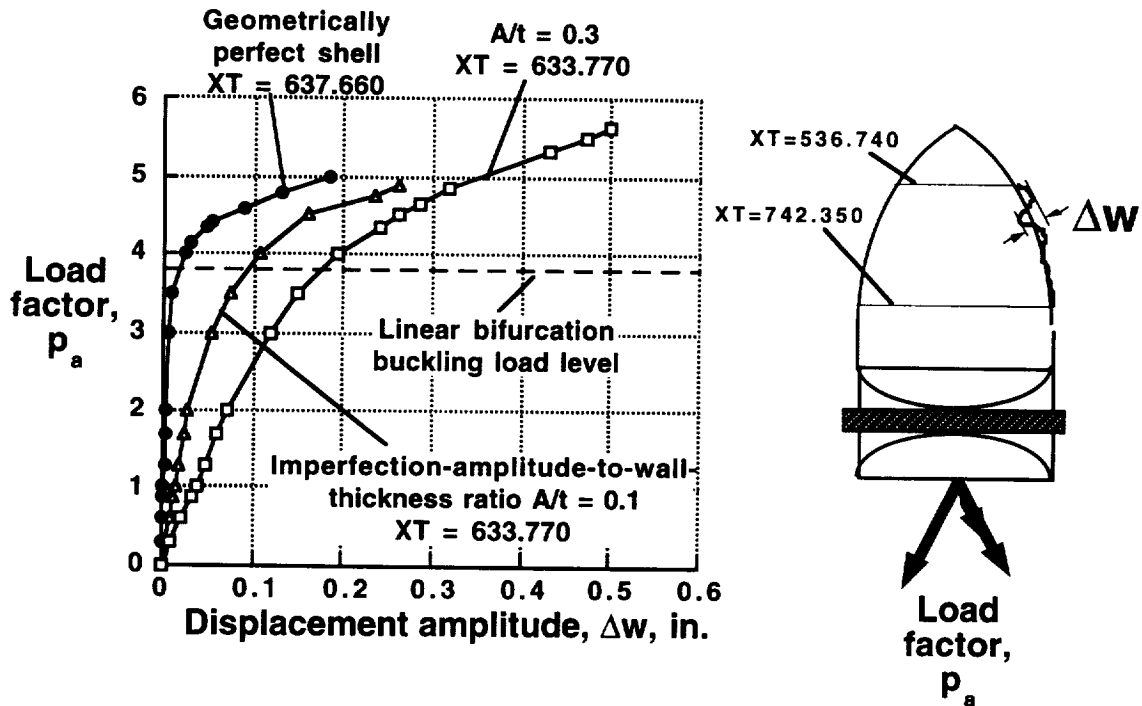


Fig. 14 Effect of imperfection amplitude on the nonlinear solutions for the prelaunch loading condition with full LH₂ and LO₂ tanks ($\theta = 270^\circ$).

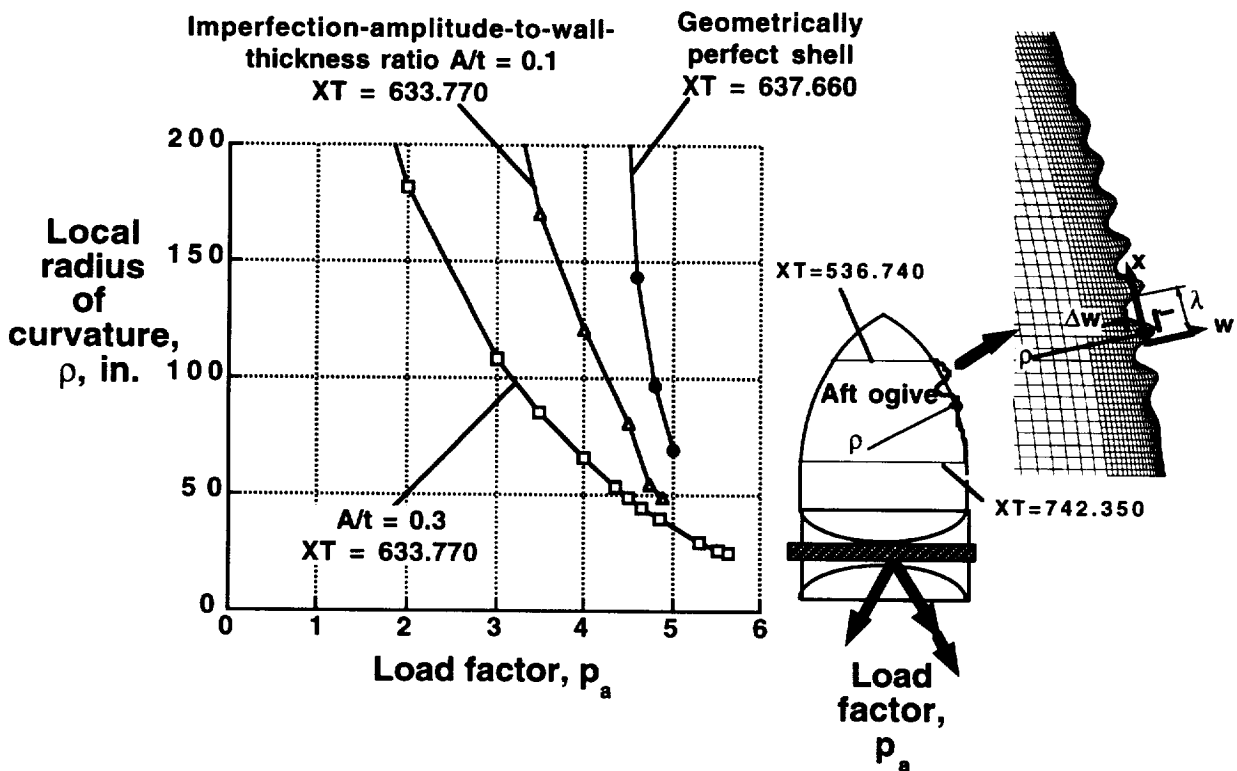


Fig. 15 Effect of imperfection amplitude on the local radius of curvature of the largest bending gradient for the prelaunch loading condition with full LH₂ and LO₂ tanks ($\theta = 270^\circ$).

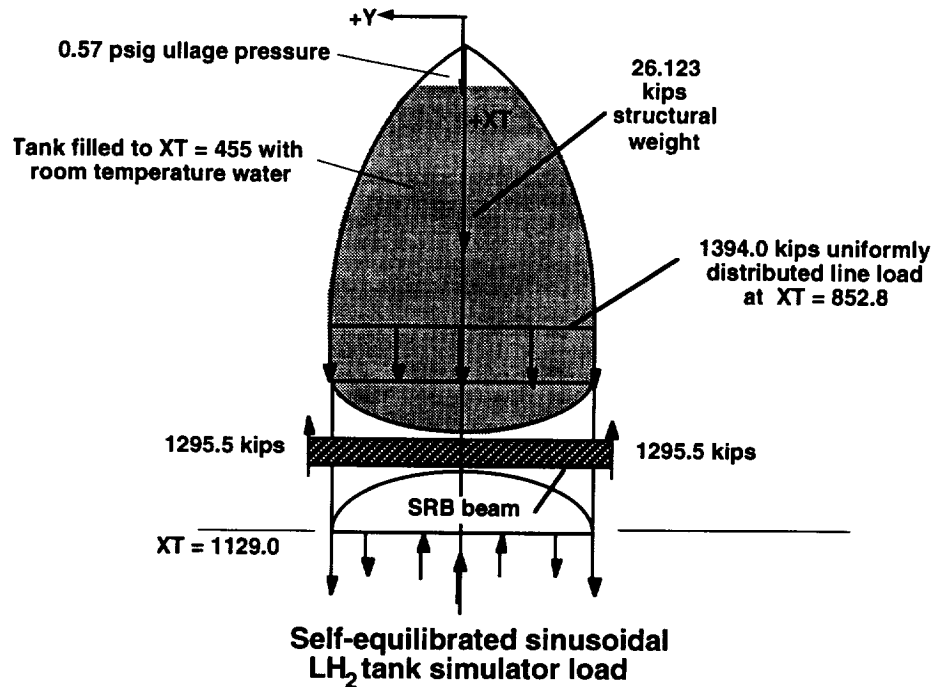


Fig. 16 Loads for standard-weight tank structural test article (STA) at buckling.

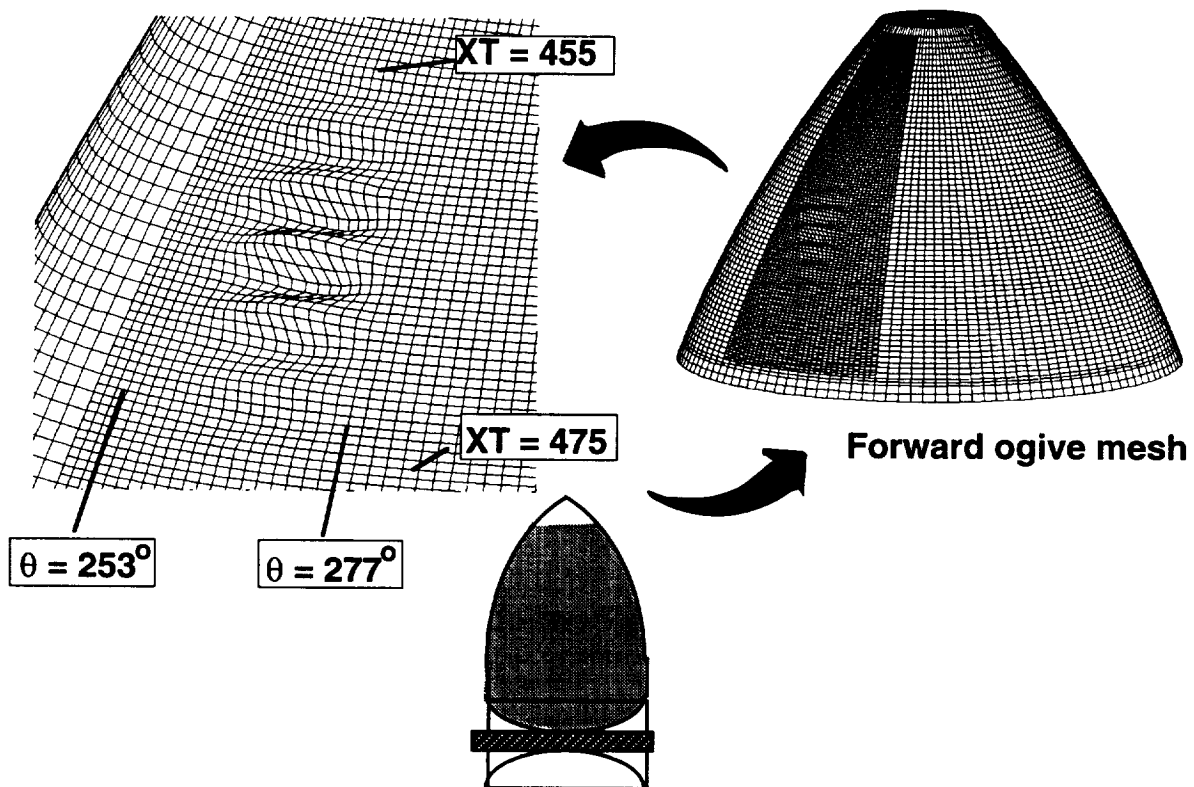


Fig. 17 Linear bifurcation buckling mode (159,993 degrees of freedom) for the structural test article (STA).

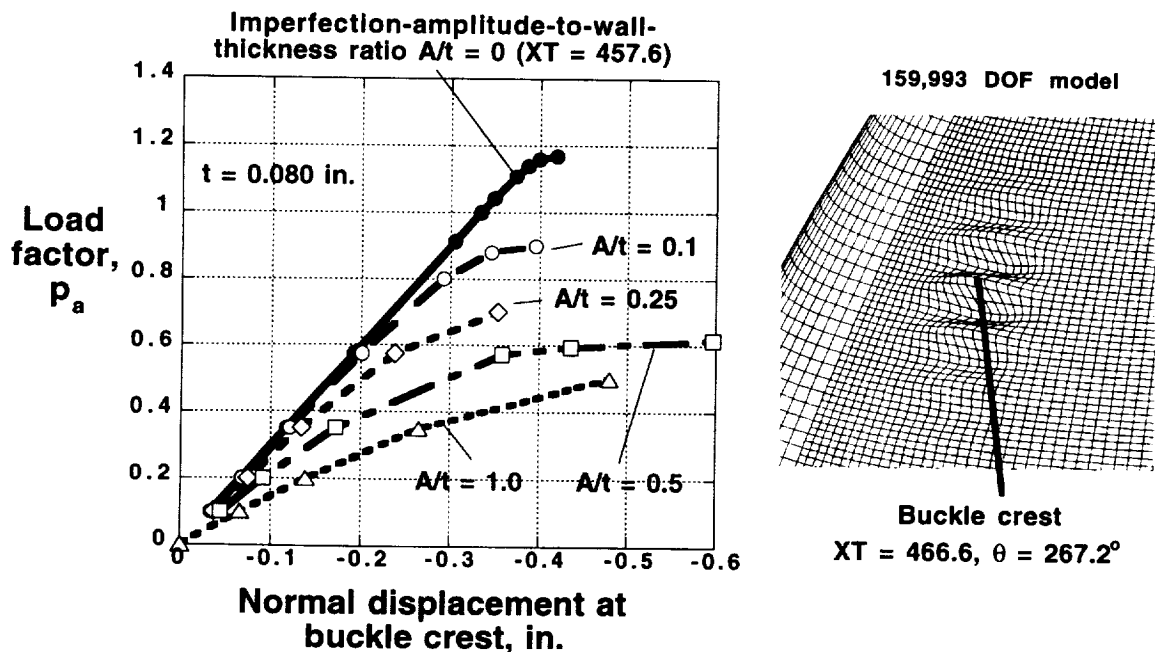


Fig. 18 Effect of imperfection amplitude on the collapse load for the structural test article (STA).

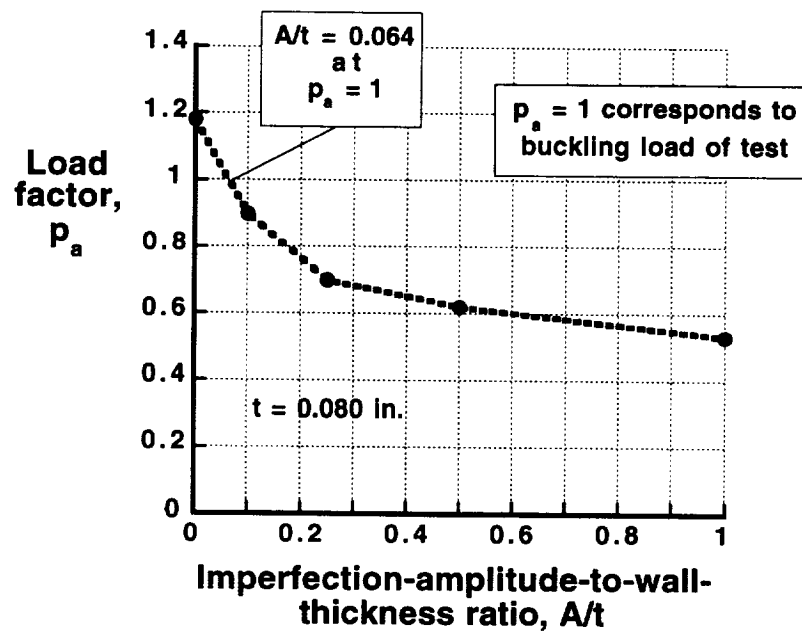


Fig. 19 Predicted imperfection sensitivity of the structural test article (STA).

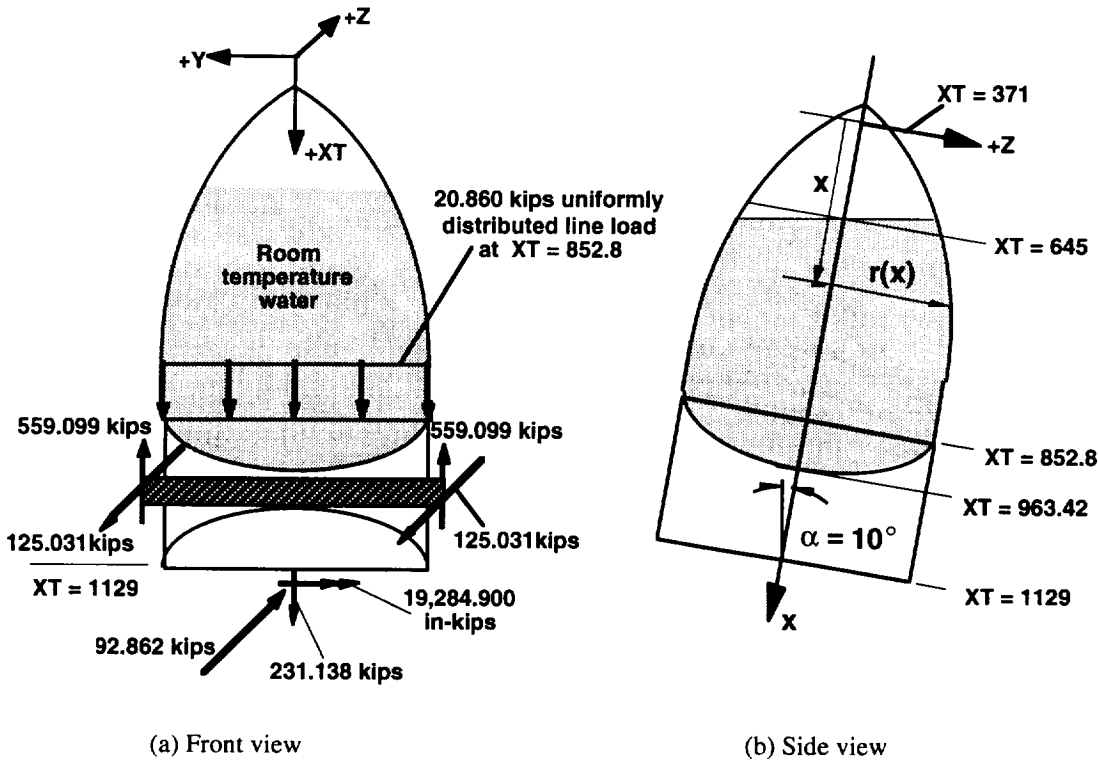


Fig. 20 Loads for standard-weight tank ground vibration test article (GVTA) at buckling.

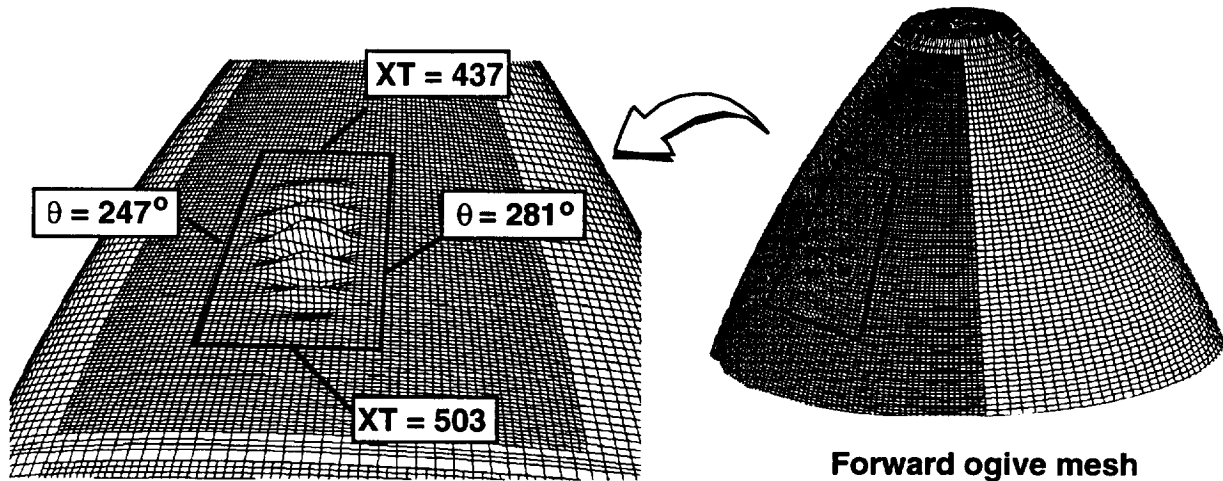


Fig. 21 Linear bifurcation buckling mode (252,300 degrees of freedom) for the ground vibration test article (GVTA).

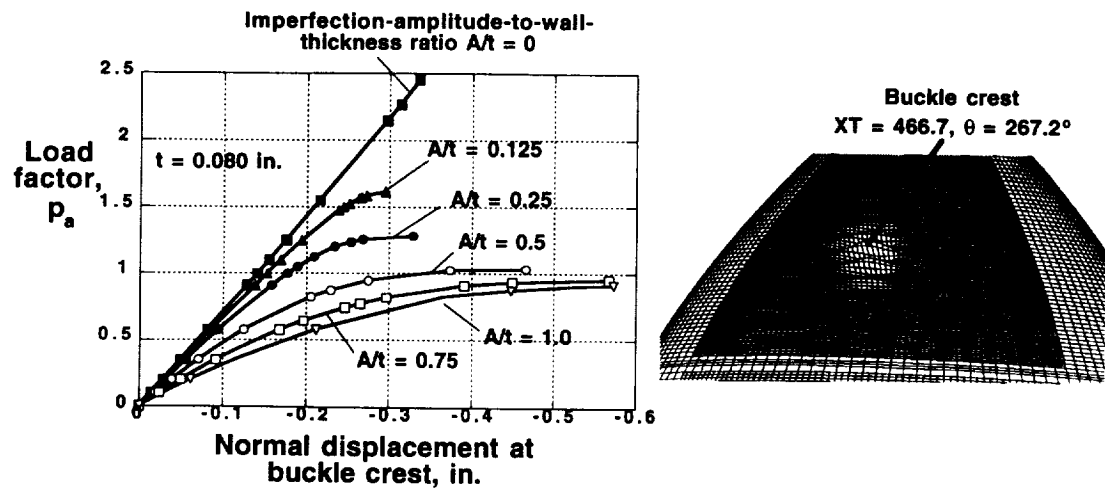


Fig. 22 Effect of imperfection amplitude on the buckling load for the ground vibration test article (GVTA).

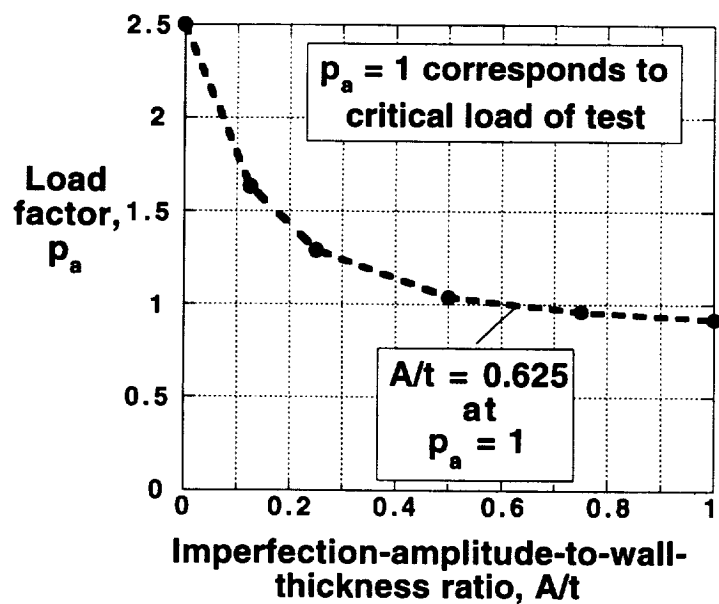


Fig. 23 Predicted imperfection sensitivity of the ground vibration test article (GVTA).